Supporting Information

Design of Crystalline Reduction–Oxidation Cluster–Based Catalysts for Artificial Photosynthesis

Xiao-Xin Li[1, 2], Lei Zhang[3], Jiang Liu[1, 3*], Lin Yuan[3], Tong Wang[3], Jun-Yi Wang[3], Long-Zhang Dong[3], Kai Huang[2] & Ya-Qian Lan[1, 3*]

[1]School of Chemistry, South China Normal University, Guangzhou 510631, China.

[2]School of Chemistry and Chemical Engineering, Southeast University, Nanjing 211189, China.

[3]Jiangsu Collaborative Innovation Centre of Biomedical Functional Materials, Jiangsu Key Laboratory of New Power Batteries, School of Chemistry and Materials Science, Nanjing Normal University, Nanjing, 210023, China.

Xiao-Xin Li and Lei Zhang contributed equally to this work.

Correspondence and requests for materials should be addressed to J. L. (email: liuj@njnu.edu.cn); Y.-Q. L. (email: yqlan@m.scnu.edu.cn; yqlan@njnu.edu.cn; Homepage: http://www.yqlangroup.com).

Experimental Procedures

Materials

All starting materials, reagents and solvents used in experiments were commercially available, high-grade purity materials and used without further purification. Piperazine ($C_4H_{10}N_2$, 99%), phosphorous acid (H_3PO_3, 98%), manganese chloride tetrahydrate ($MnCl_2·4H_2O$, 99%) and zinc chloride ($ZnCl_2$, 98%) were purchased from Adamas, 1,4-di(4H-1,2,4-triazol-4-yl)benzene (*p*-tr_2Ph, 97%) was purchased from Jinan Henghua Technology Co., Ltd., Phosphomolybdic acid hydrate ($H_3PMo_{12}O_{40}·xH_2O$, 98%), phosphoric acid (H_3PO_4, 85%), sodiummolybdate dihydrate ($Na_2MoO_4·2H_2O$, 99%), cobaltous chloride hexahydrate ($CoCl_2·6H_2O$, 99%) and ammonium vanadate (NH_4VO_3, 99%) were purchased from Sinopharm Chemical Reagent Co. Ltd., Nickel chloride hexahydrate ($NiCl_2·6H_2O$, 99%) were purchased from Aladdin.

Instrumentation

Thermogravimetric analyses (TGA) of the samples were performed on a Perkin–Elmer TG-7 analyzer heated from room temperature to 800 °C in flowing N_2/O_2 with a heating rate of 10 °C/min. Fourier transform infrared spectroscopy (FTIR) was recorded in the range of 4000-400 cm^{-1} on a Mattson Alpha-Centauri spectrometer using the technique of pressed KBr pellets. Powder X-Ray diffraction (PXRD) measurements were recorded ranging from 5 to 50° at room temperature on a D/max 2500 VL/PC diffractometer (Japan) with equipped with graphite mono-chromatized Cu Kα radiation (λ = 1.54060 Å). The ultraviolet-visible-near infrared (UV-VIS-NIR) spectra were acquired on a Shimadzu UV-2550 spectrophotometer in the wavelength range of 250–2500 nm. X-ray photoelectron spectroscopy (XPS) and ultraviolet photoelectron spectroscopy (UPS) were measured on an Escalab 250Xi. The data of XPS spectra are already referenced to C 1s at 284.6 eV. PL spectra were recorded by a FluoroMax-4 spectrofluorometer (HORIBA Scientific). The gases (CO, CH_4 and H_2) were detected and analyzed by gas chromatography (GC) (GC-7900, CEAULIGHT) equipped with a flame ionization detector (FID, couple with a TDX-01 packed column) and a thermal conductivity (TCD, couple with a TDX-01 packed column). The hydrocarbon products were detected by a gas chromatography-mass spectrometry (7890B and 5977B, Aglient) coupled with a HP PLOT-Q capillary column (Agilent). Electrochemical measurements (transient photocurrent response, the Mott–Schottky spots) were using an electrochemical workstation CHI 660E. Inductively coupled plasma-optical emission spectroscopy (ICP-OES) was measured on Agilent-720. Elemental analyses of C, N and H were performed on an elementar Vario EL cube.

Single-Crystal X-ray Analyses.

The diffraction data of **RO- 1, 2, 3** were collected on Bruker AXS Apex II CCD diffractometer (Mo Kα, λ = 0.71069 Å) at 293 K.[1] The crystal structures were solved and refined by full matrix least-squares methods against F^2 using the SHELXL-2014[2, 3] program package and Olex-2 software.[4] All non-hydrogen atoms were refined with anisotropic displacement parameters and hydrogen positions were fixed at calculated positions and refined isotropically. The crystallographic data and structure refinement for **RO-1, 2, 3** is summarized in Table S1. CCDC 2052416-2052418 (**RO-1, 2, 3**) contain the supplementary crystallographic data for the paper. These data can be obtained free of charge from The Cambridge Crystallographic Data Centre.

Apparent quantum yield

Φ_{CO} = [2×(number of the produced molecule) / (number of photons)] ×100%

Light intensity (I) = 32.4 mW/cm^2. Area (S) = 3.14 cm^2

photon flux = (I×S) / (h×c / λ) = 2.87×10^{-7} mol/s where h is Planck constant = 6.626×10^{-34} J·s, c is velocity of light = 3.373×10^{8} m/s, λ = 380 nm.

After 10 hours, 0.53 μmol, 0.38 μmol and 0.14 μmol CO produced when **RO-1, 2, 3** were utilized as photocatalysts respectively. Then the Φ_{CO} of **RO-1, 2, 3** were calculated to be 0.0103%, 0.00738% and 0.00272%.

Photocatalyst	**RO-1**	**RO-2**	**RO-3**
Φ_{CO} (%)	0.0103	0.00738	0.00272

Table S1. Crystal data and structure refinement of **RO-1, 2, 3**.

	RO-1	**RO-2**	**RO-3**
Empirical formula	$C_{50}H_{60}Zn_3Mo_9N_{30}O_{54}PV_7$	$C_{50}H_{64}Co_3Mo_9N_{30}O_{56}PV_7$	$C_{50}H_{57}Ni_3Mo_9N_{30}O_{52.5}PV_7$
Formula weight	3394.42	3411.13	3341.36
Temperature/K	296.15	296.15	296.15
Crystal system	Triclinic	Triclinic	Triclinic
Space group	*P*-1	*P*-1	*P*-1
a/Å	13.251(3)	13.192(6)	13.192(3)
b/Å	13.815(4)	13.827(7)	13.829(4)
c/Å	15.234(4)	15.235(7)	15.232(4)
α/°	64.881(2)	64.679(5)	64.737(3)
β/°	80.952(3)	81.023(6)	81.014(3)
γ/°	72.986(3)	73.062(6)	72.843(3)
Volume/Å^3	2412.8(11)	2401(2)	2397.9(11)
Z	1	1	1
ρ_{calc} g/cm^3	2.336	2.359	2.312
μ/mm^{-1}	2.625	2.410	2.476
F(000)	1648.0	1659.0	1621.0
Reflections collected	19324	10519	19370
Independent reflections	10392[R_{int} = 0.0195, R_{sigma} = 0.0350]	10519 [R_{sigma} = 0.0635]	10331 [R_{int} = 0.0235, R_{sigma} = 0.0381]
Data/restraints/parameters	10392/0/715	10519/18/742	10331/864/789
Goodness-of-fit on F^2	1.046	1.041	1.066
Final R indexes [I>=2σ (I)]	R_1 = 0.0452, wR_2 = 0.1308	R_1 = 0.0545, wR_2 = 0.1469	R_1 = 0.0415, wR_2 = 0.1133
Largest diff. peak/hole / e Å^{-3}	1.95/-1.47	1.54/-1.35	1.34/-0.95

$^a R_1 = \Sigma||F_o| - |F_c||/\Sigma|F_o|$. $^b wR_2 = |\Sigma w (|F_o|^2 - |F_c|^2)|/\Sigma|w(F_o^2)^2|^{1/2}$

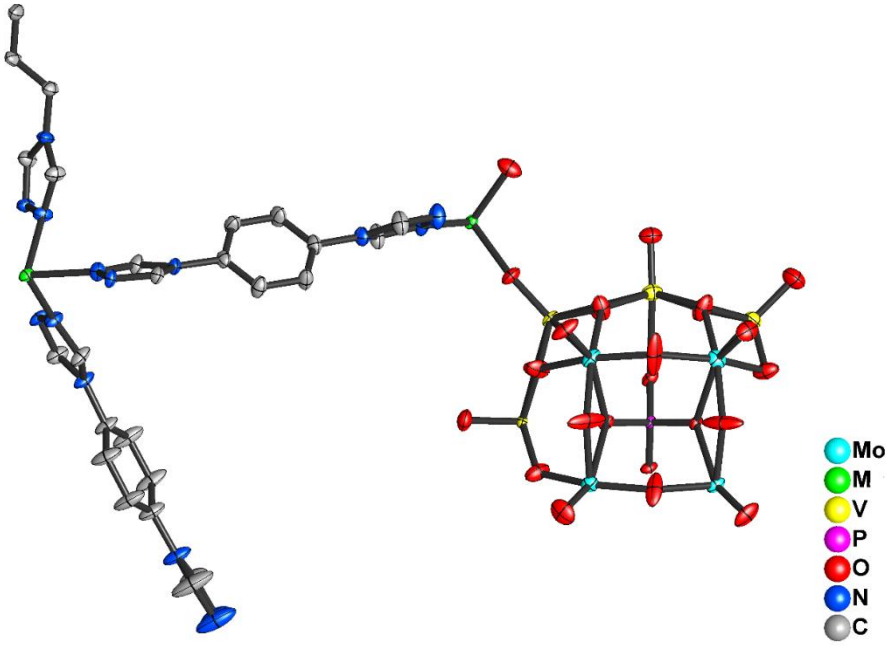

Figure S1. The asymmetric unit of **RO-1, 2, 3** with thermal ellipsoids at 50% probability displacement. All hydrogen atoms and free water molecules are omitted for clarity. Mo, cyan; M = Zn, Co, Ni, green; V, yellow; P, pink; O, red; N, blue; C, gray.

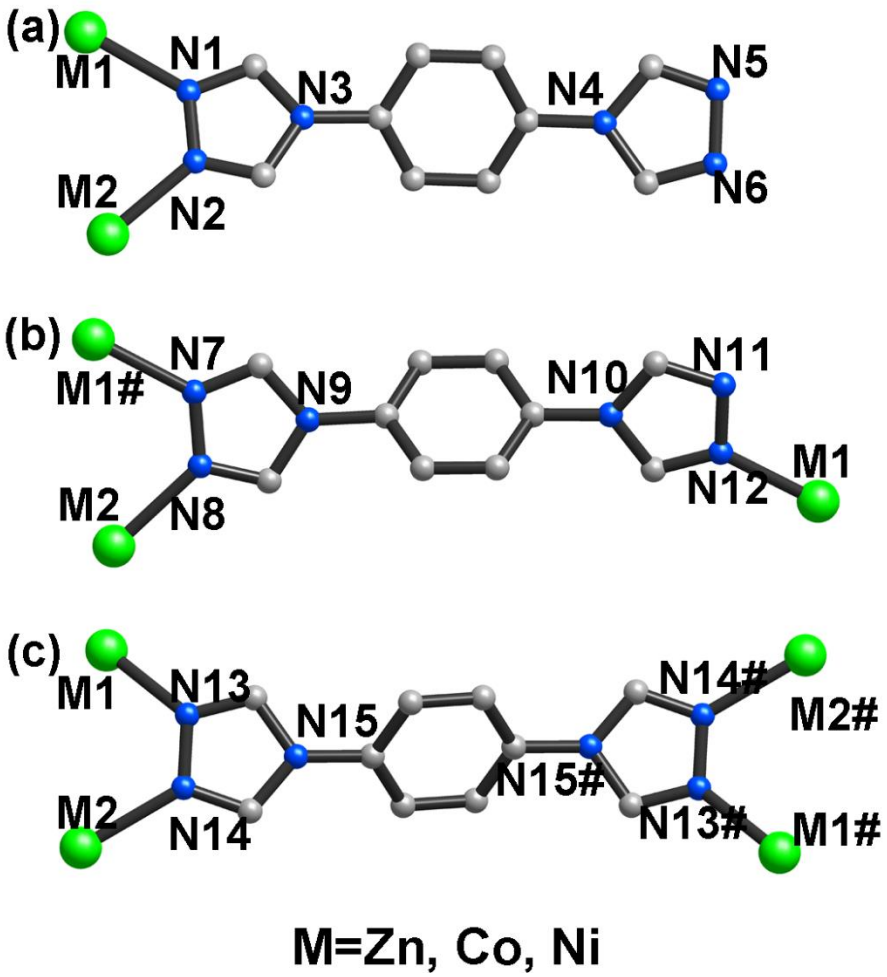

Figure S2. The coordination environment of ligands in **RO-1, 2, 3**.
The environment of ligands have three kinds coordination environments. (a) Two N atoms (N1 and N2) coordinate with two M (M1 and M2) ions, N5 and N6 are uncoordinated. (b) three N (N7, N8 and N12) atoms coordinate with three M (M1#, M2 and M1) ions, N11 are uncoordinated. (c) Four N (N13, N14, N13# and N14#) atoms coordinate with four M (M1, M2, M1# and M2#) ions by symmetry. All hydrogen atoms are omitted for clarity. C, gray; M, green; N, blue.

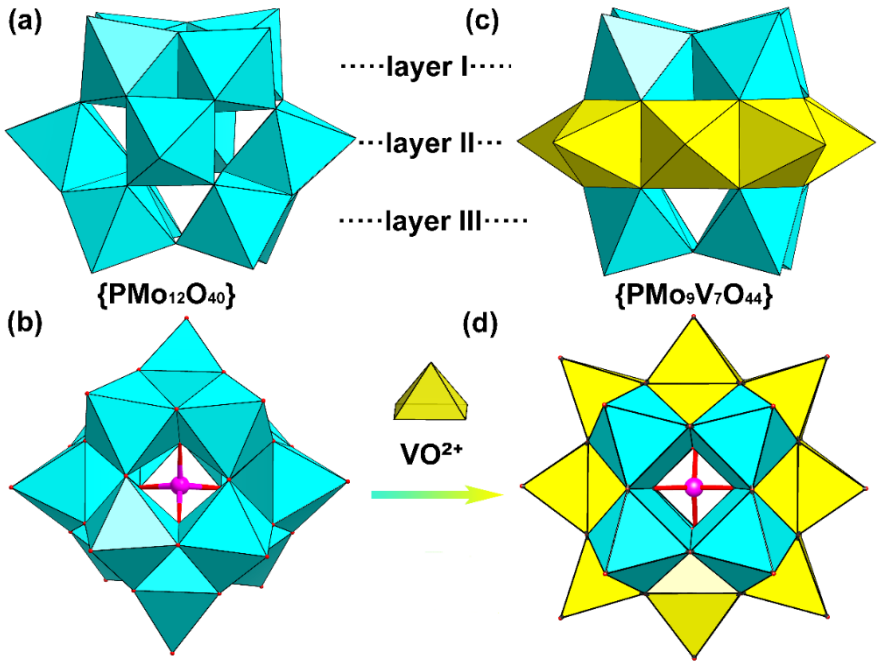

Figure S3. (a), (b) Polyhedral of $\{PMo_{12}O_{40}\}$ Keggin structure. (c), (d) Polyhedral of $\{PMo_9V_7O_{44}\}$ structure. $\{VO_5\}$, yellow; $\{MoO_6\}$, cyan. The disorder atoms of Mo and V are also labelled yellow.

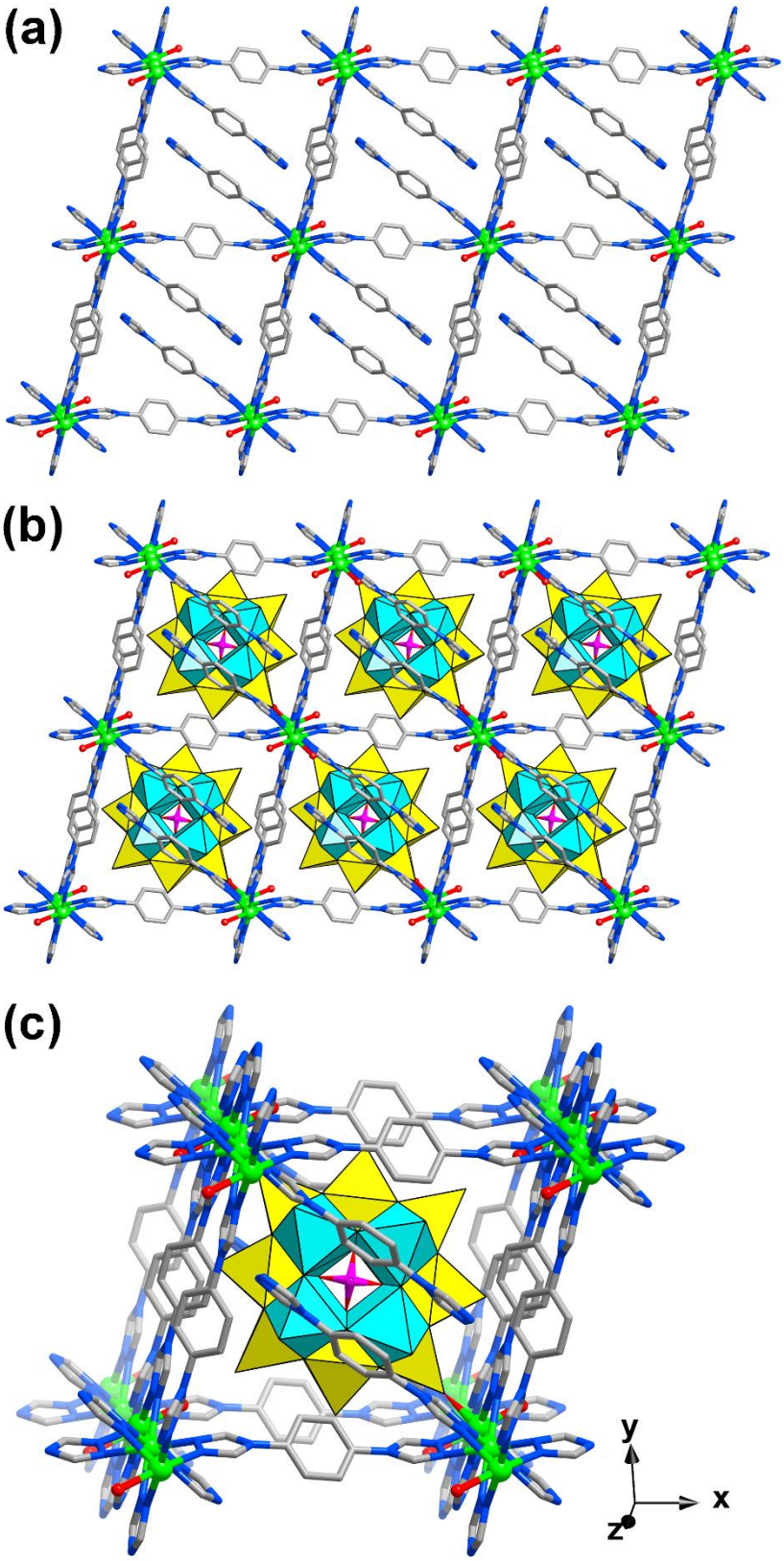

Figure S4. (a) 2D layer structure constructed from {**M**$_3$} clusters and *p*-tr$_2$Ph ligands along *c* axis. (b) {PMo$_9$V$_7$O$_{44}$} clusters embedded in 2D layers. (c) the coordination environment diagram of one {PMo$_9$V$_7$O$_{44}$} cluster.

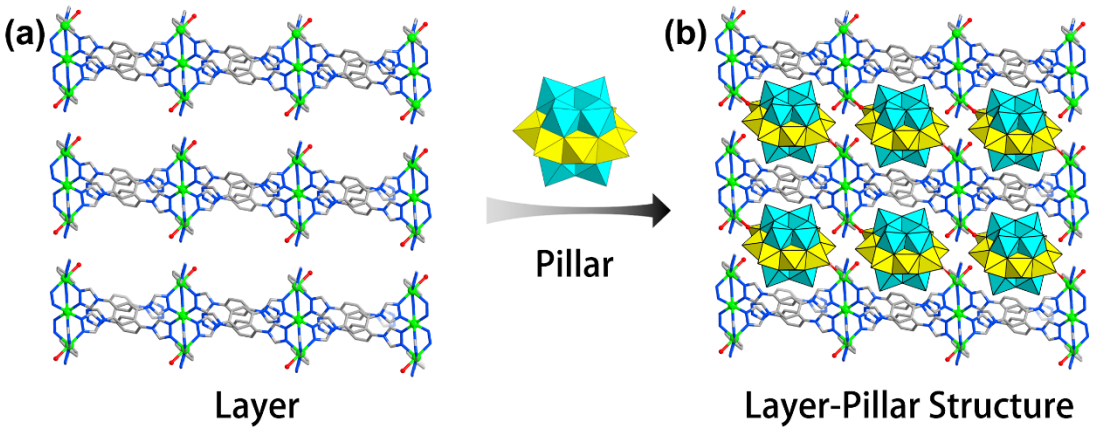

Figure S5. (a) 2D layers consist of {$\mathbf{M_3}$} clusters. (b) POMs as pillars supports the layers to form a 3D layer-pillar structure. All hydrogen atoms are omitted for clarity. {MoO_6}, cyan; {VO_5}, yellow; M = Zn, Co, Ni, green; O, red; N, blue; C, gray.

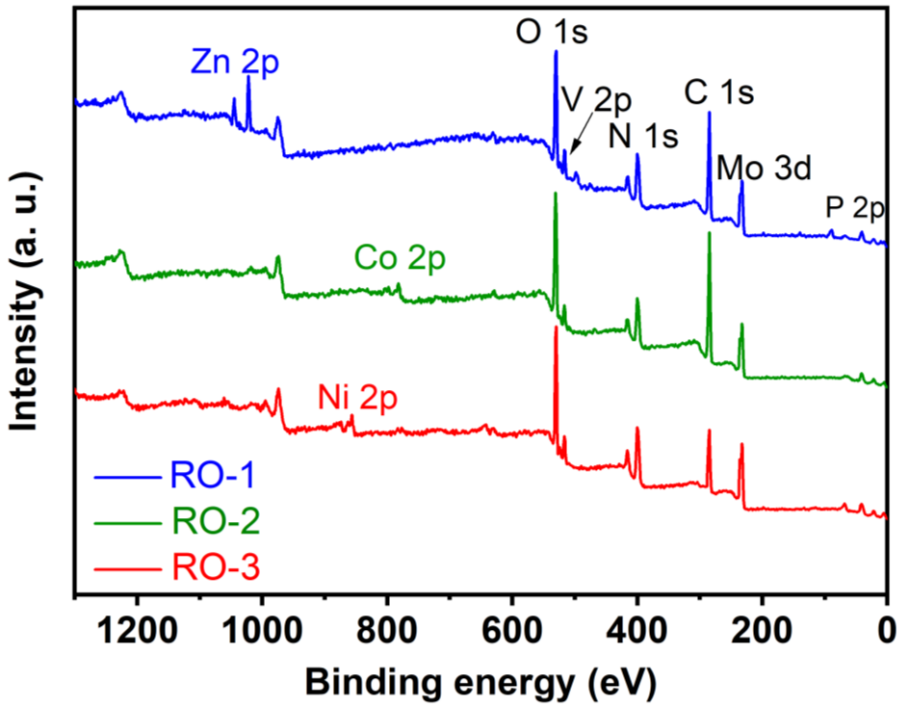

Figure S6. XPS spectra of **RO-1, 2, 3**.
The Zn 2p spectrum of **RO-1** (blue curve) shows two main peaks at 1022.08 eV and 1045.08 eV which ascribed to Zn^{II} $2p_{3/2}$ and $2p_{1/2}$, respectively. The Co 2p spectrum of **RO-2** (green curve) shows two main peaks at 782.08 eV and 798.08 eV, which ascribed to Co^{II} $2p_{3/2}$ and $2p_{1/2}$, respectively. The Ni 2p spectrum of **RO-3** (red curve) shows two main peaks at 856.08 eV and 874.08 eV, which ascribed to Ni^{II} $2p_{3/2}$ and $2p_{1/2}$, respectively.

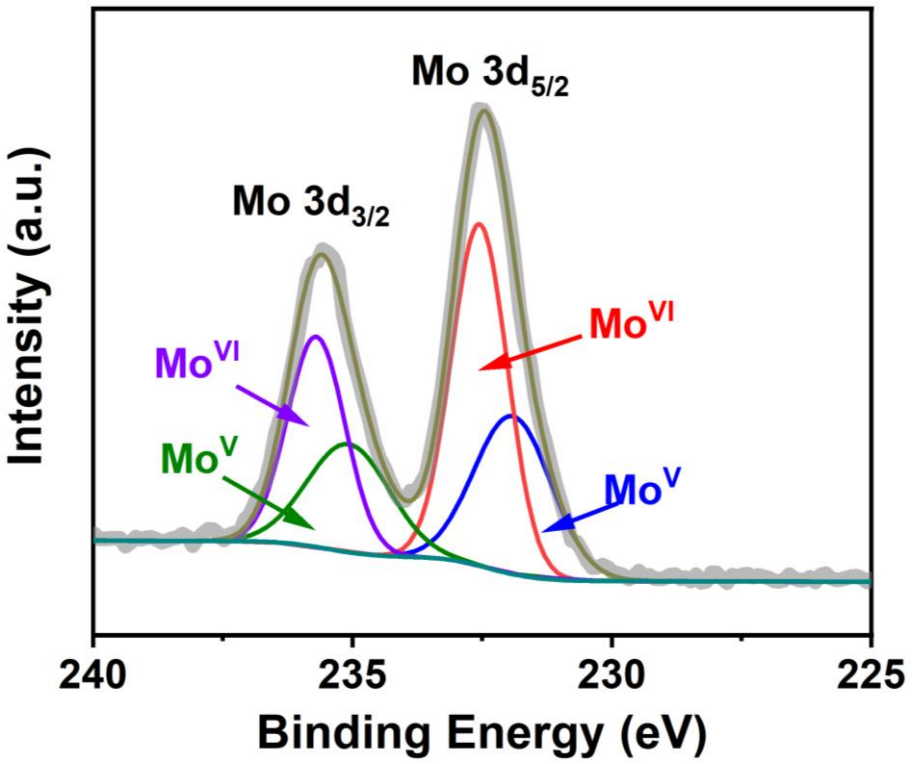

Figure S7. High-resolution peaks of Mo 3d spectrum of **RO-1**.
The Mo 3d spectrum shows two main peaks at 232.5 eV and 235.5 eV which can be deconvoluted into four peaks at 231.9 eV, 232.6 eV, 235.1 eV and 235.7 eV, ascribed to Mo^{V} $3d_{5/2}$ and Mo^{VI} $3d_{5/2}$, Mo^{5+} $3d_{3/2}$ and Mo^{6+} $3d_{3/2}$, respectively.

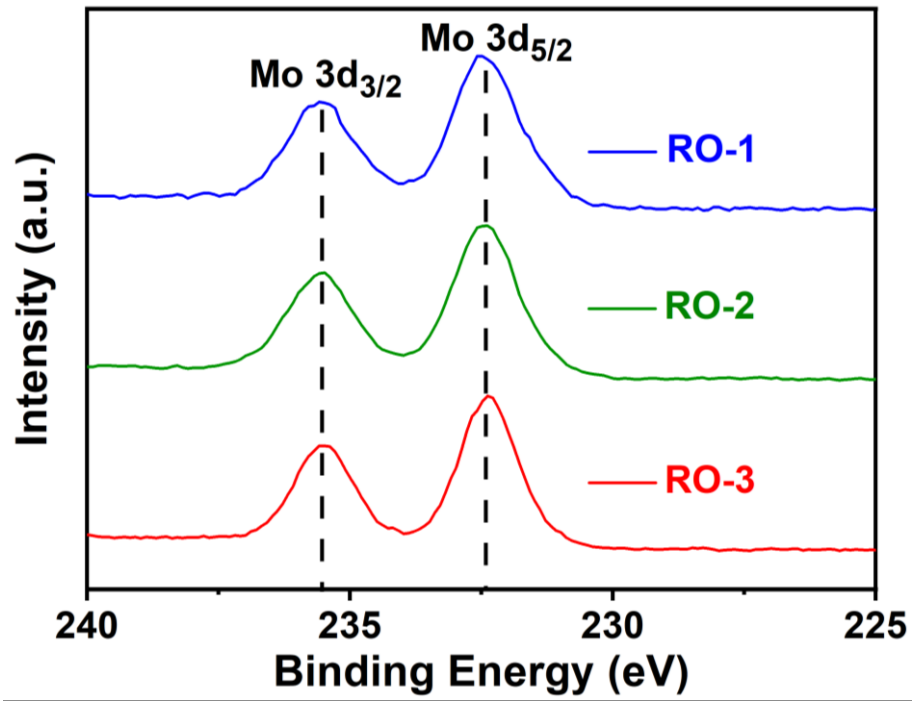

Figure S8. Mo 3d XPS spectra of **RO-1, 2, 3** in survey scan.

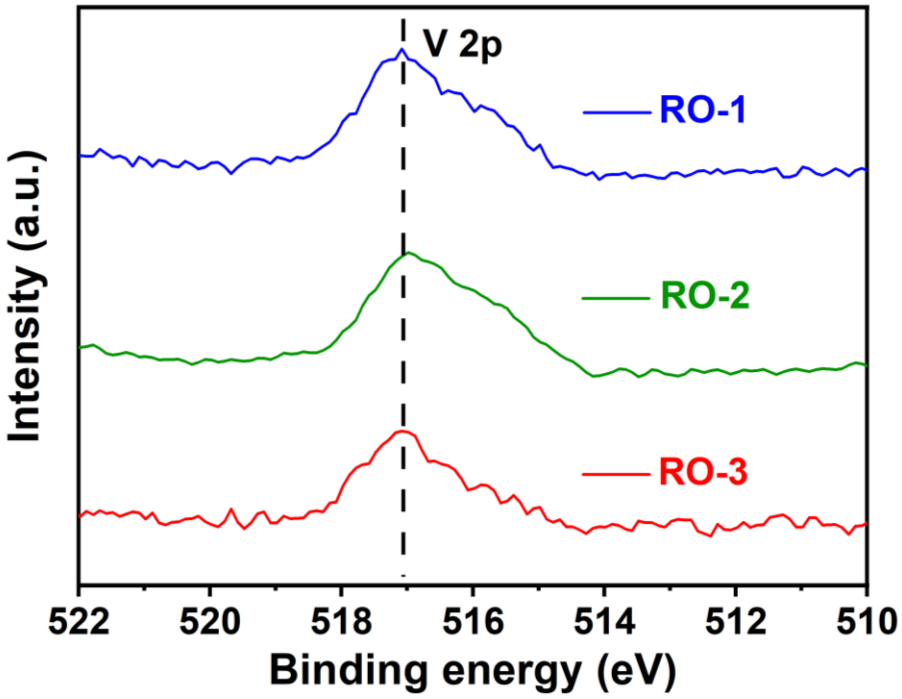

Figure S9. V 2p XPS spectra of **RO-1, 2, 3** in survey scan.

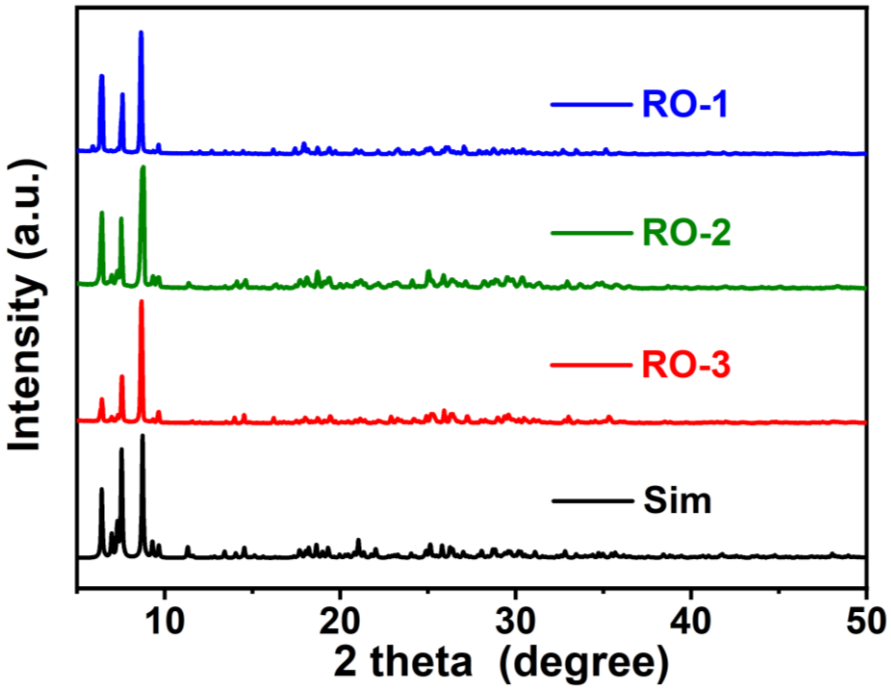

Figure S10. The PXRD patterns of experimental **RO-1, 2, 3** and simulated curves.

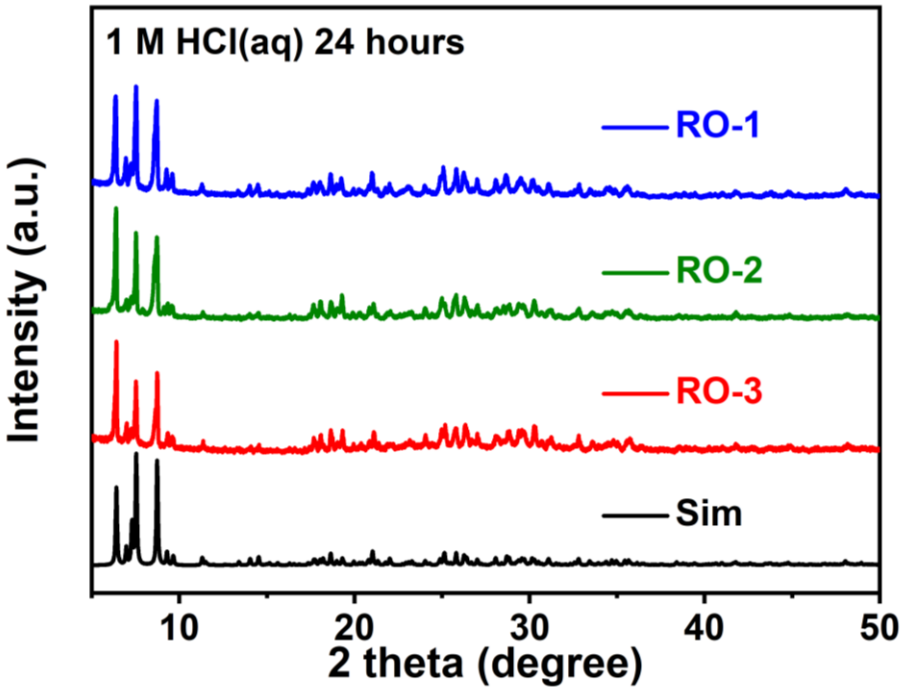

Figure S11. The PXRD patterns of **RO-1, 2, 3** in 1 M HCl aqueous solution after 24 hours and simulated curves.

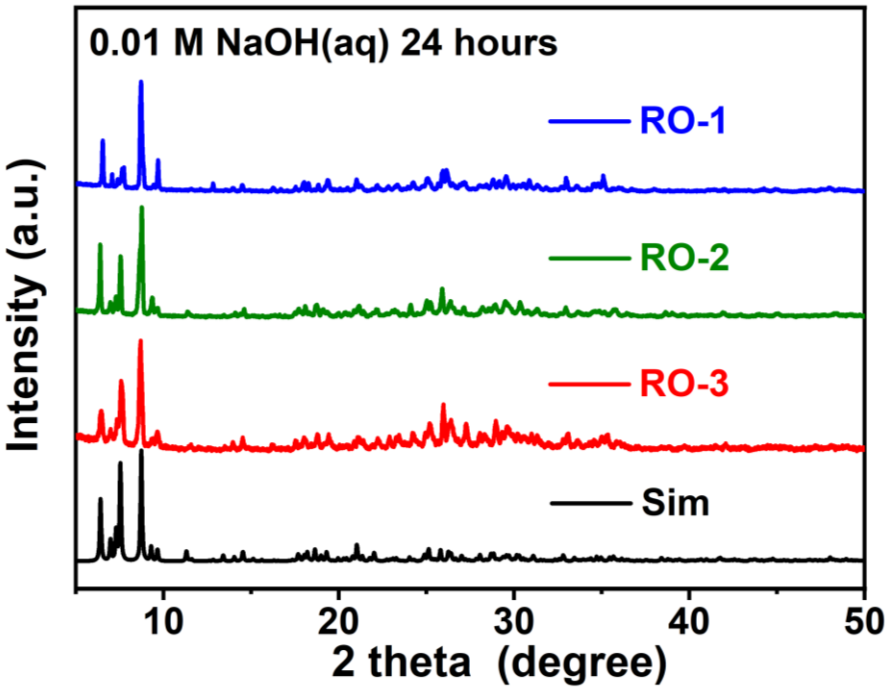

Figure S12. The PXRD patterns of **RO-1, 2, 3** in 0.01 M NaOH aqueous solution after 24 hours and simulated curves.

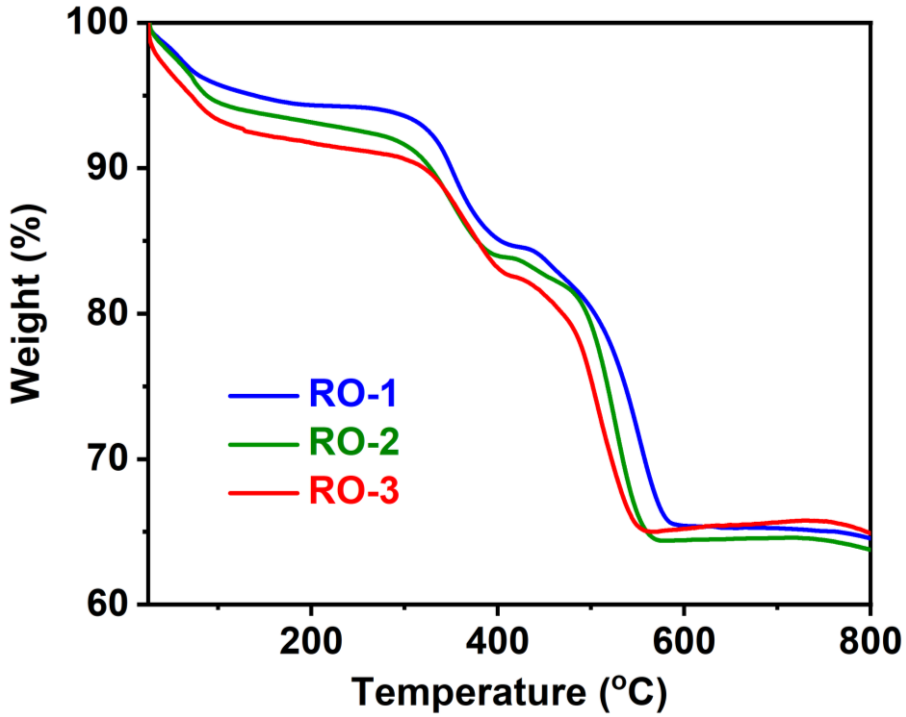

Figure S13. The TGA curves of **RO-1, 2, 3** measured in N_2/O_2 from room temperature to 800 °C at the heating rate of 10 °C·min^{-1}.

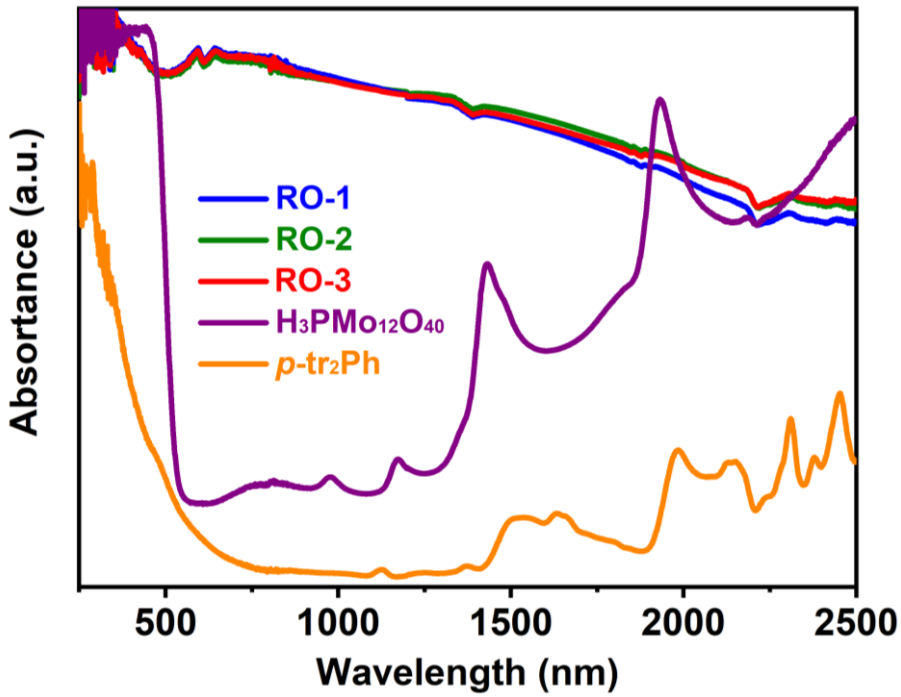

Figure S14. UV-Vis absorption of **RO-1** (blue curve), **RO-2** (green curve) **RO-2** (red curve), $H_3PMo_{12}O_{40}\cdot xH_2O$ (mulberry curve) and *p*-tr_2Ph (organic curve). **RO-1, 2, 3** could largely extend the light response from ultraviolet light even to infrared light with wavelengths up to 2500 nm.

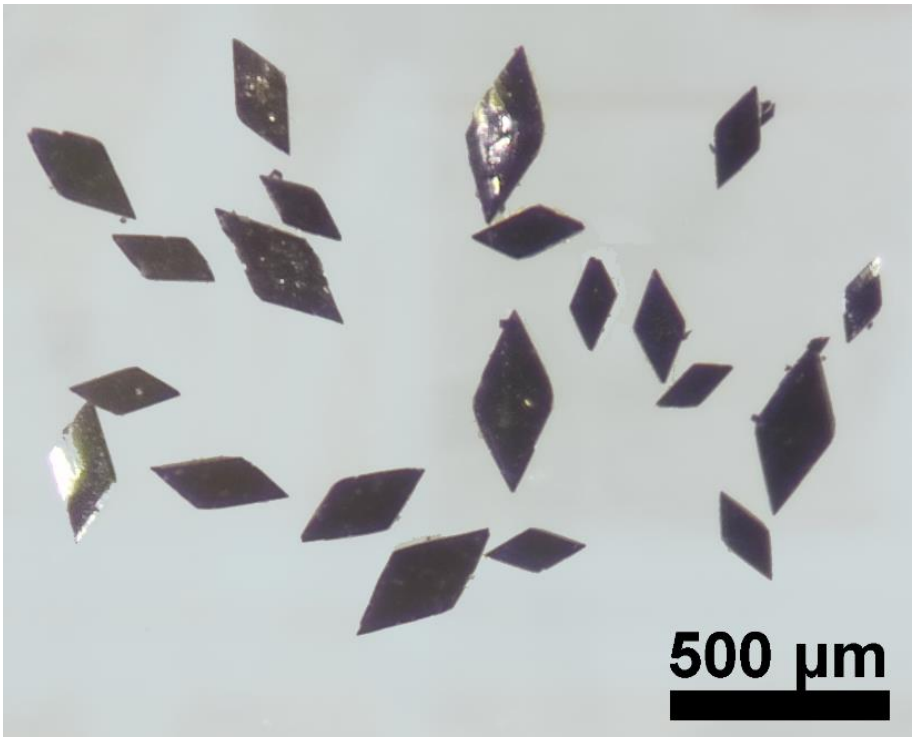

Figure S15. The photograph of **RO-2** under an optical microscope.

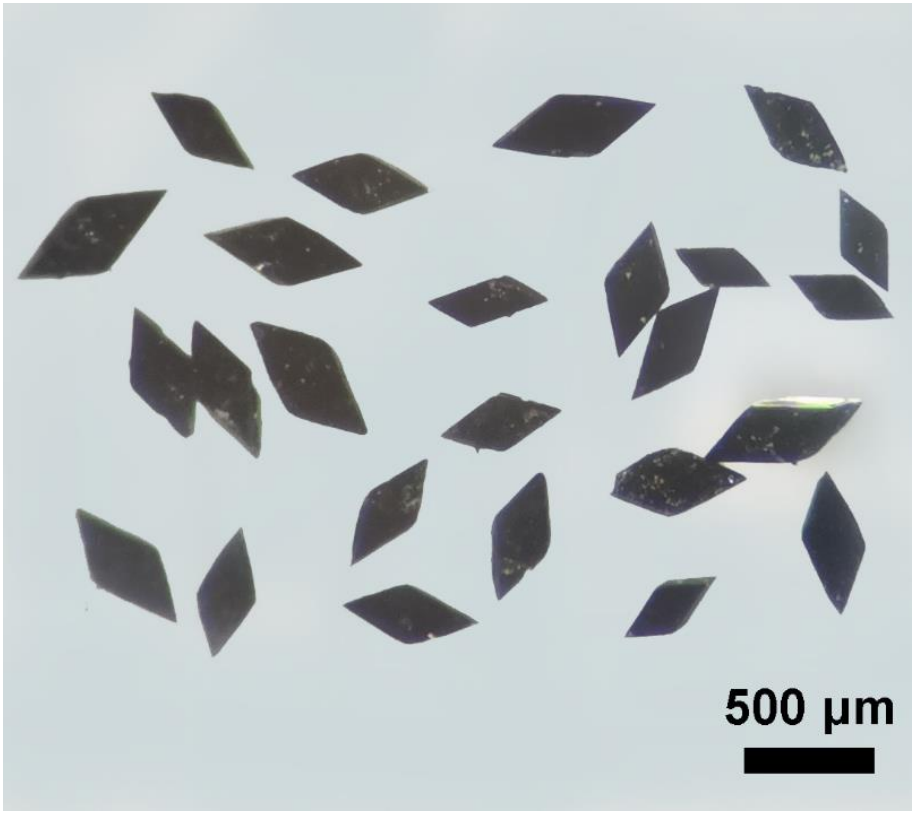

Figure S16. The photograph of **RO-3** under an optical microscope.

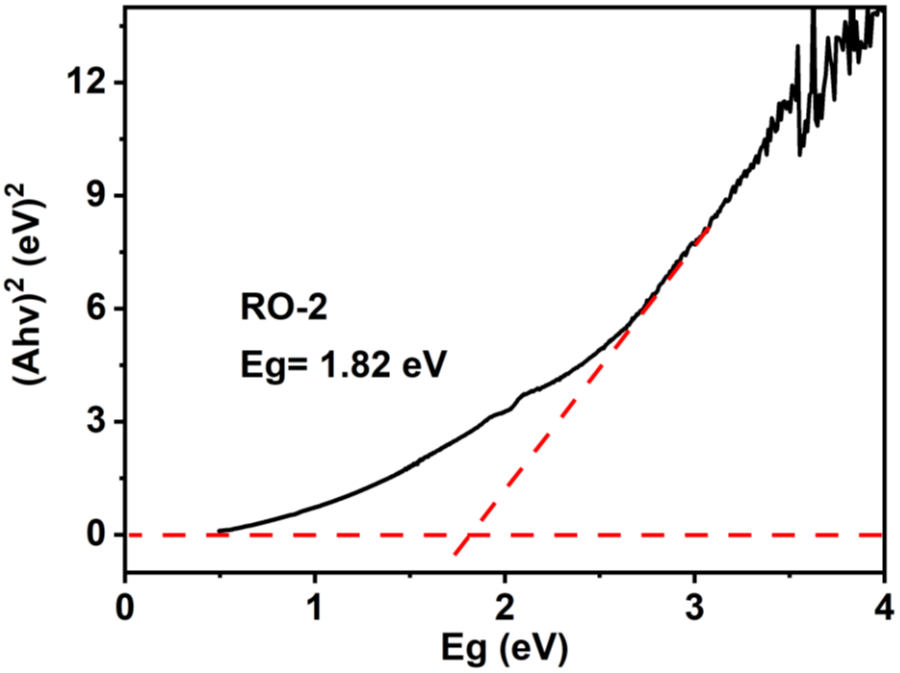

Figure S17. The band gap energy (Eg) analysis of **RO-2**. The intersection of baseline and slant dashed line is the band gap. Kubelka-Munk formula: ($\alpha hv = C\ (hv - E_g)^2$).

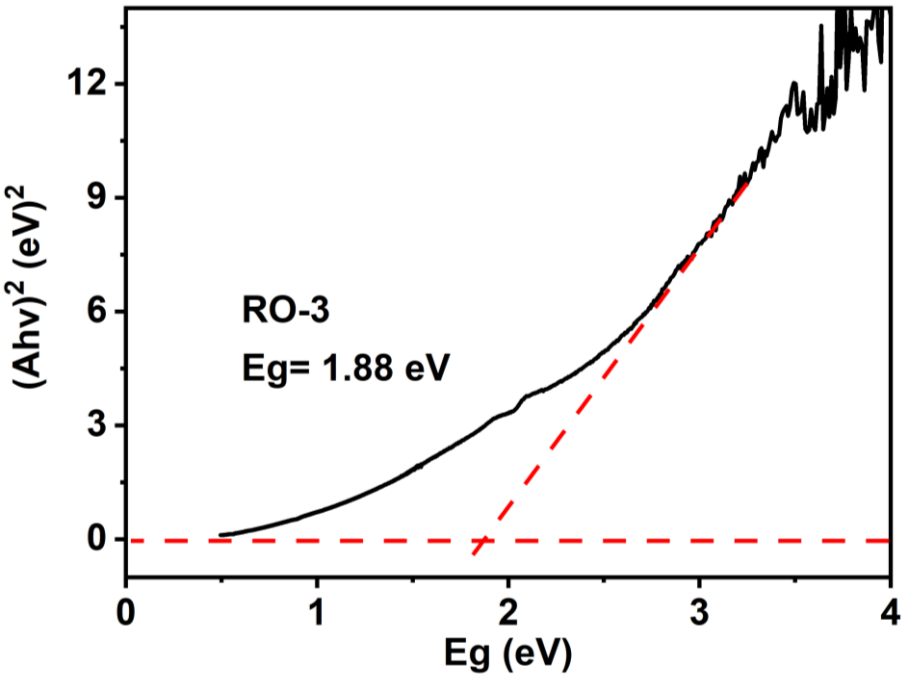

Figure S18. The band gap energy analysis of **RO-3**. The intersection of baseline and slant dashed line is the band gap.

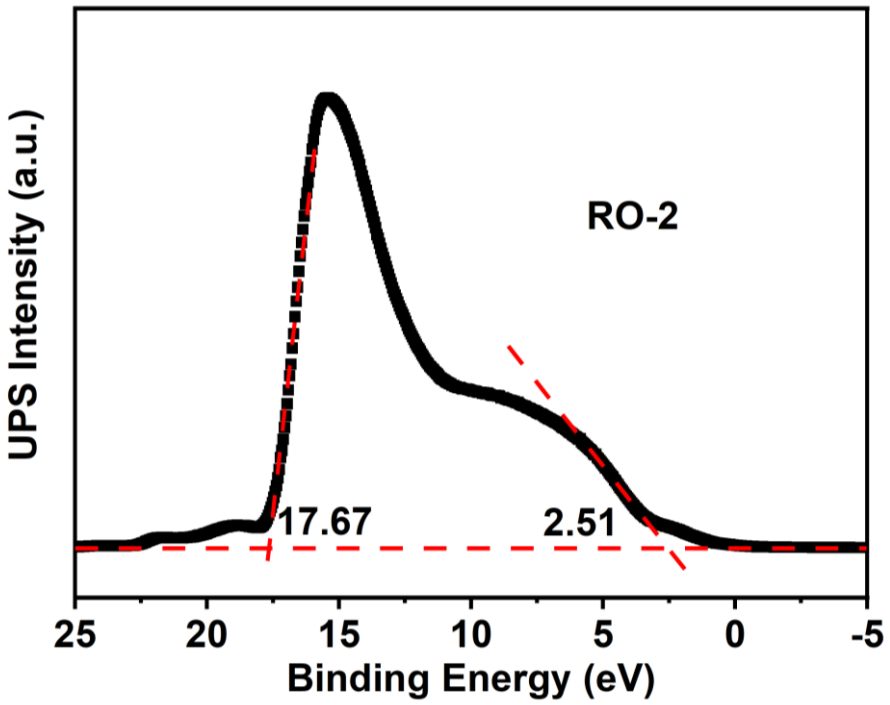

Figure S19. Ultraviolet photoelectron spectroscopy (UPS) spectrum of **RO-2**.
The flat red dotted line is the baseline, and the other two red dotted lines are tangents of the curves. The intersection points of tangent and baseline are the edge of the UPS spectrum. On this basis, the width of the He-I-UPS spectrum is 15.16 eV. Then the ionization potential [equivalent to the valence band energy (E_v)] of **RO-2** is determined at -6.06 eV since subtracting 15.16 eV from the excitation energy (21.22 eV).

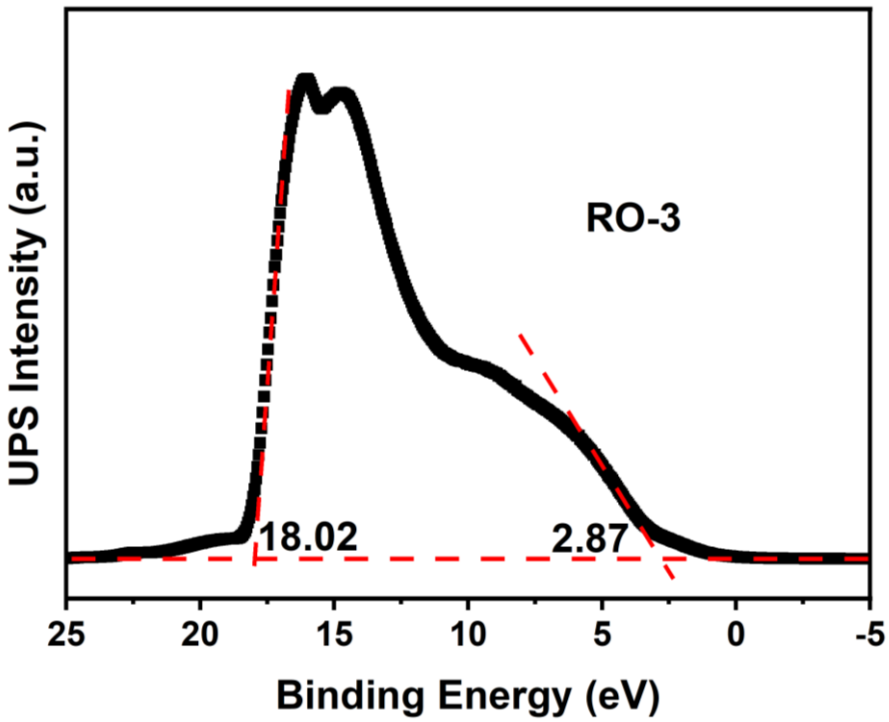

Figure S20. Ultraviolet photoelectron spectroscopy (UPS) spectrum of **RO-3**.
The width of the He I UPS spectrum is calculated to be 15.15 eV from the different of the two intersection values. Then the ionization potential of **RO-3** is determined at -6.07 eV by subtracting 15.15 eV from the excitation energy (21.22 eV).

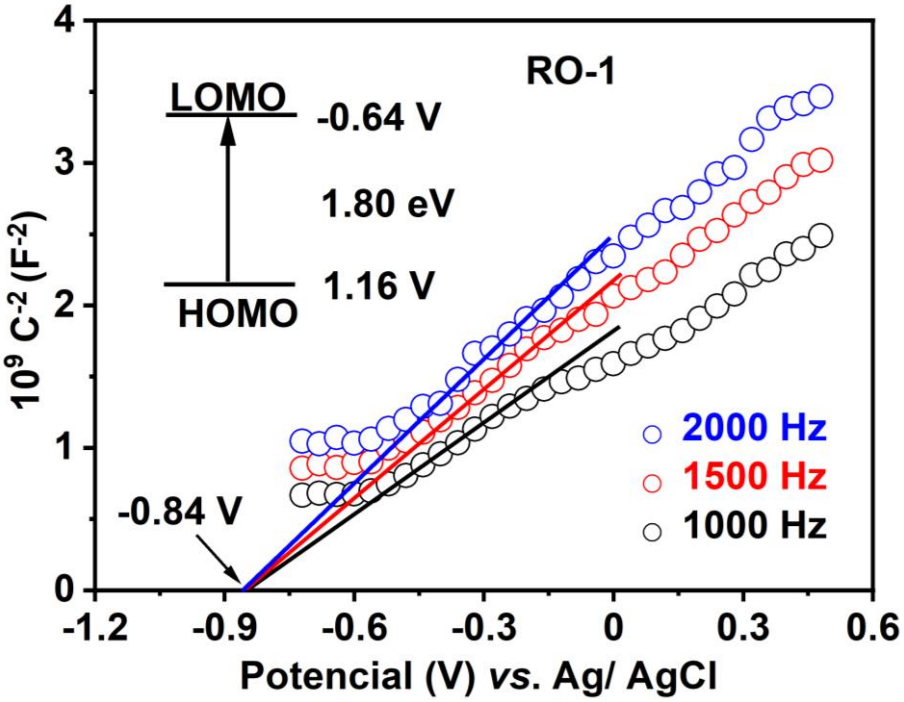

Figure S21. Mott–Schottky plot measurement for **RO-1**. Inset: Energy diagram of the Highest Occupied Molecular Orbital (HOMO) and Lowest Unoccupied Molecular Orbital (LUMO) levels of **RO-1**.

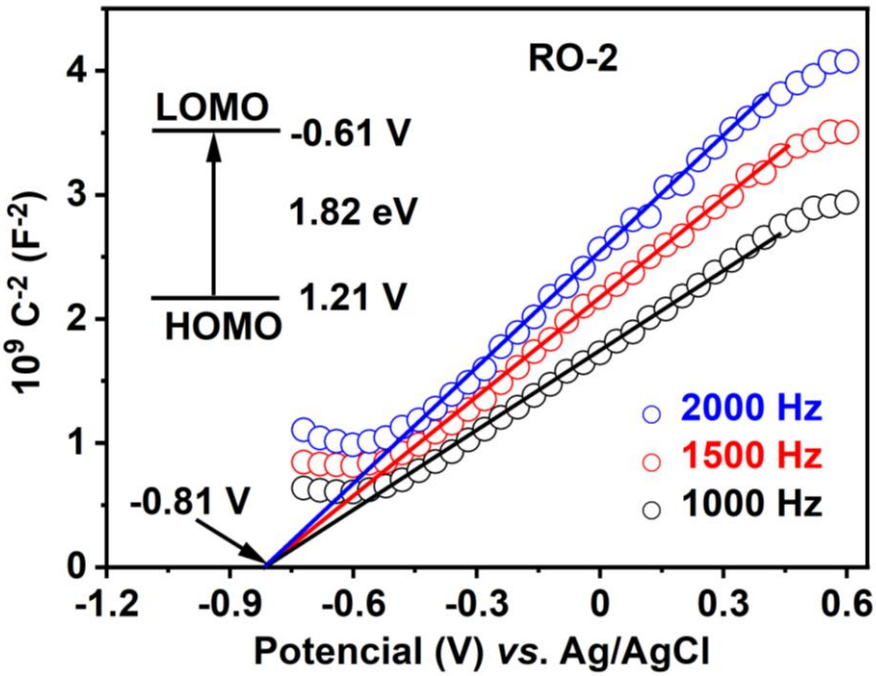

Figure S22. Mott–Schottky plot measurement for **RO-2**. Inset: Energy diagram of the HOMO and LUMO levels of **RO-2**.

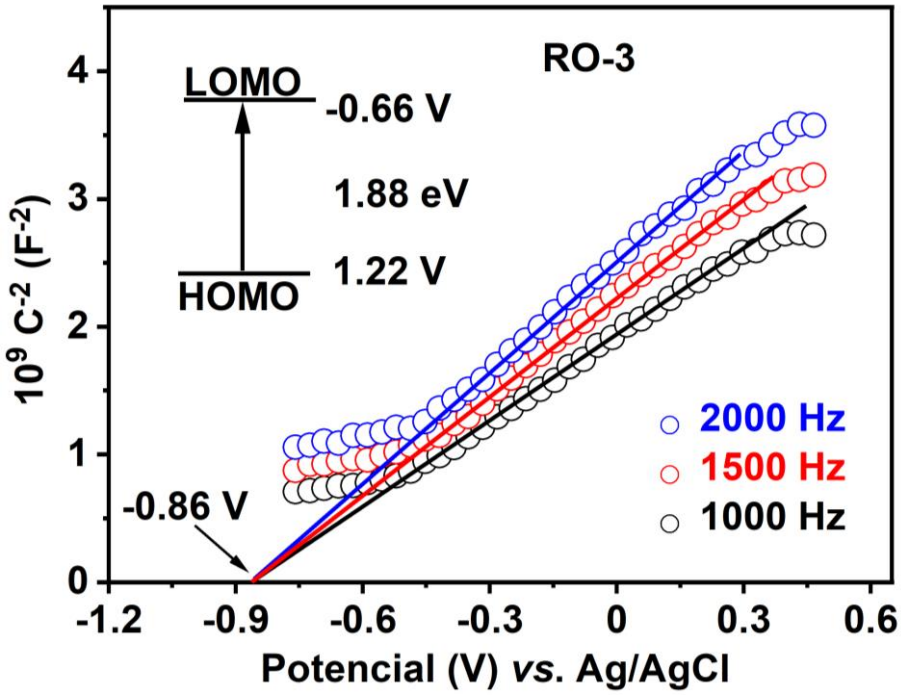

Figure S23. Mott–Schottky plot measurement for **RO-3**. Inset: Energy diagram of the HOMO and LUMO levels of **RO-3**.

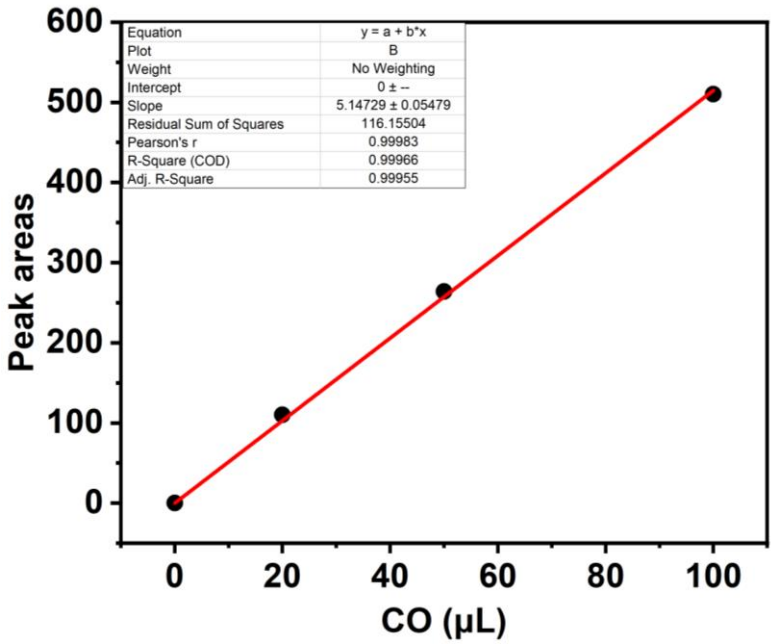

Figure S24. The standard curve is detected by FID using highly purified CO. High linearities ensure the reliability of our data.

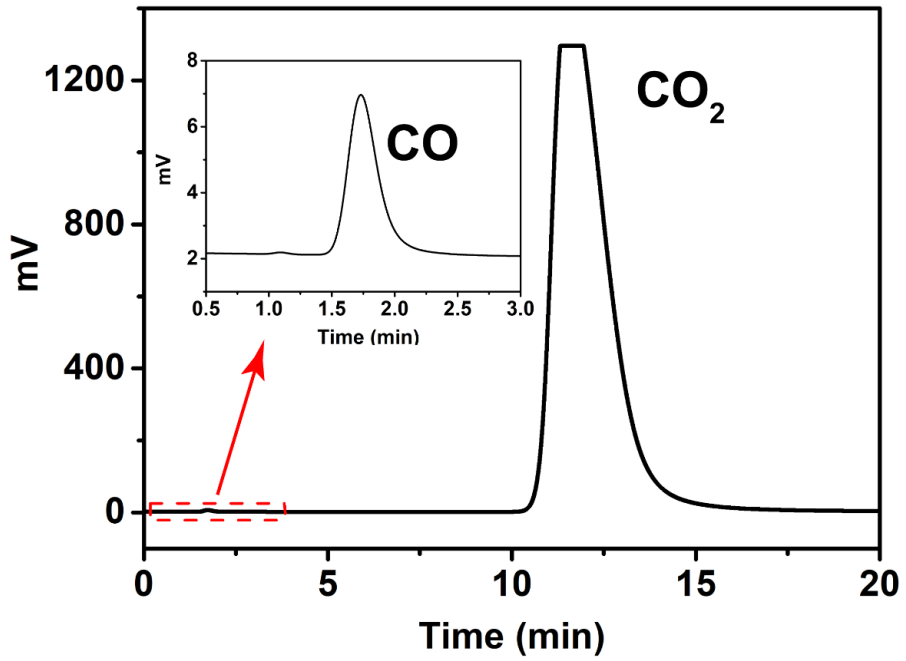

Figure S25. GC analysis of the gaseous reaction products by using FID. Inset: close-up from 0.5 to 3 min in *x* axis and from 1.00 to 8.00 mV in *y* axis.

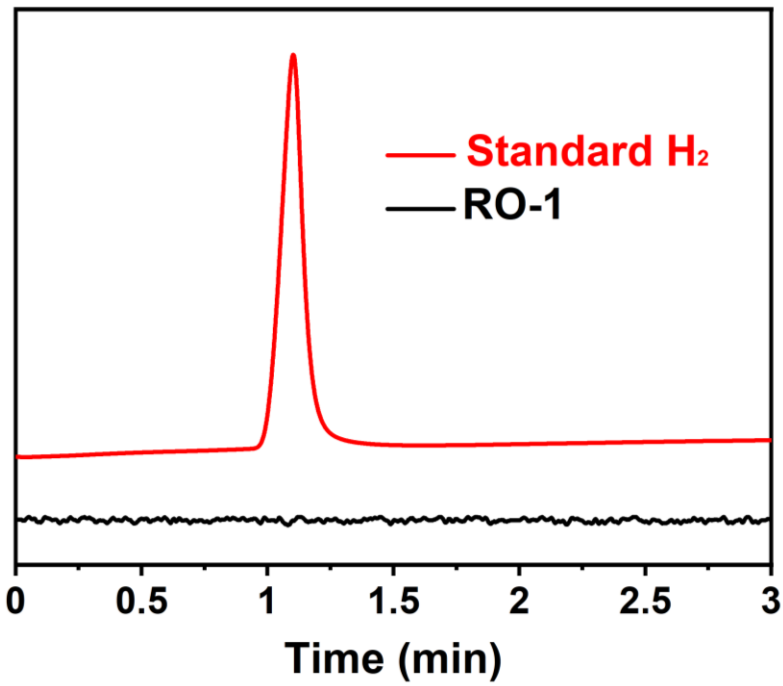

Figure S26. GC analysis of the gaseous reaction product by using the thermal conductivity detector (TCD) (red curve), **RO-1** (black curve).

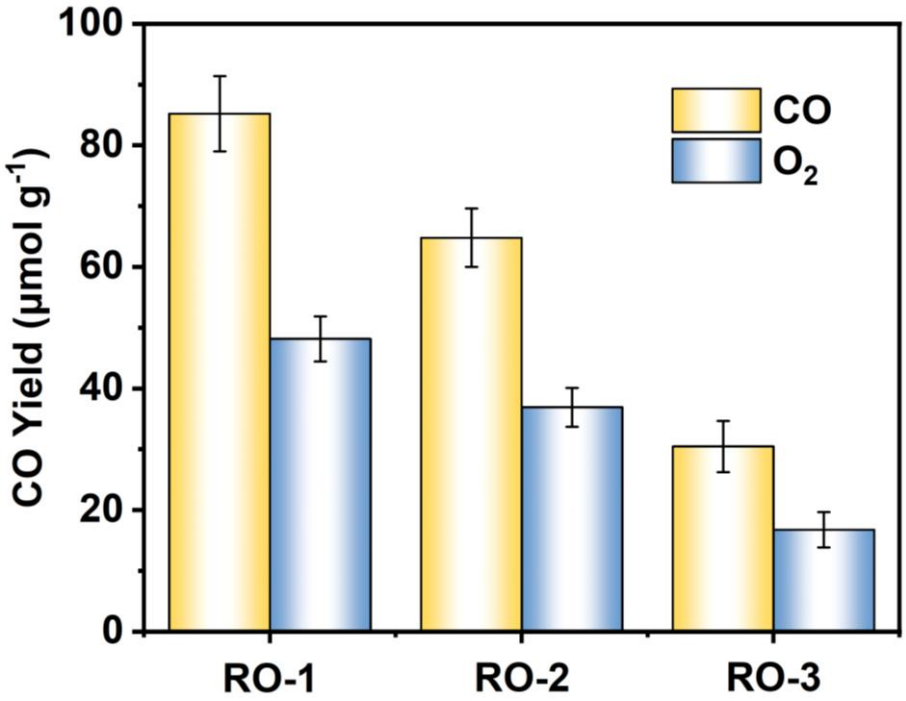

Figure S27. The comparison of CO and O_2 yield in a online evaluation system catalyzed by **RO-1, 2, 3**, respectively.

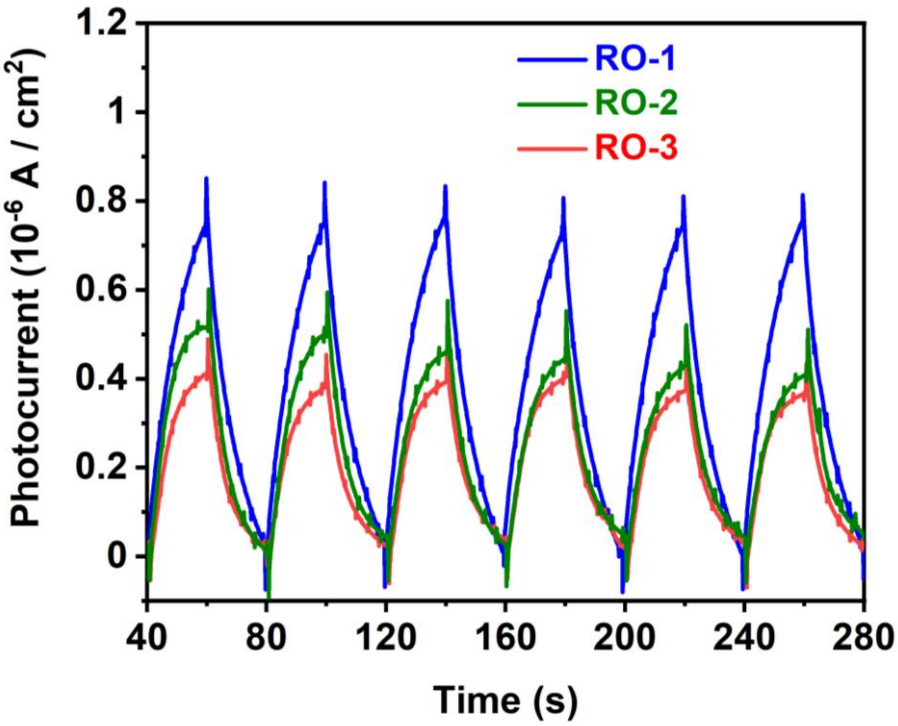

Figure S28. Transient photocurrent response of **RO-1** (blue curve), **RO-2** (green curve) and **RO-3** (orange curve),respectively. A Xenon light (300-1100 nm) was applied as the light source for photocurrent, and 0.5 M Na_2SO_4 aqueous solution was used as the electrolyte.

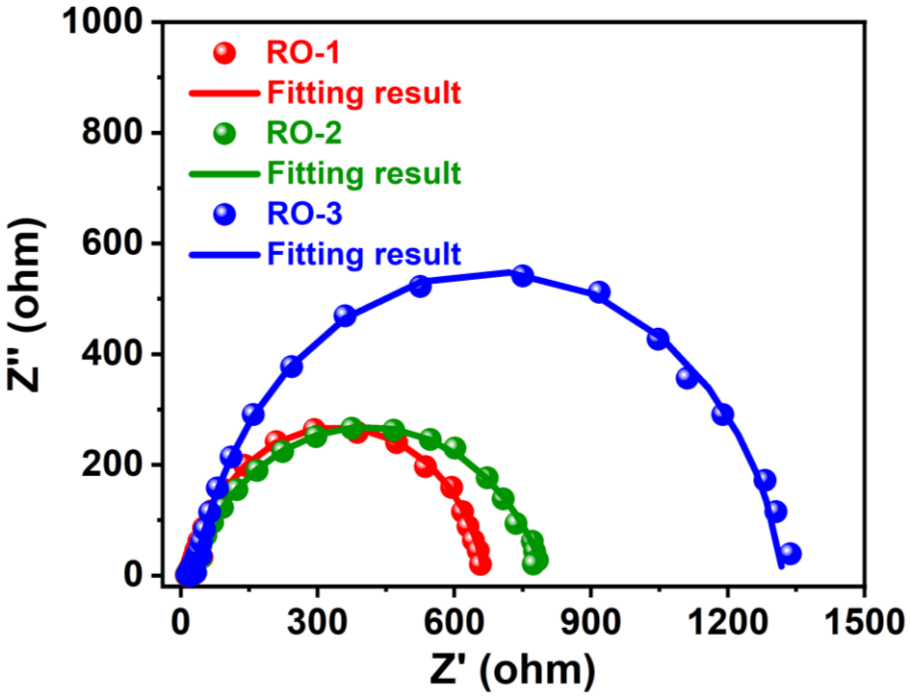

Figure S29. EIS Nyquist plots of **RO-1, 2, 3** respectively.

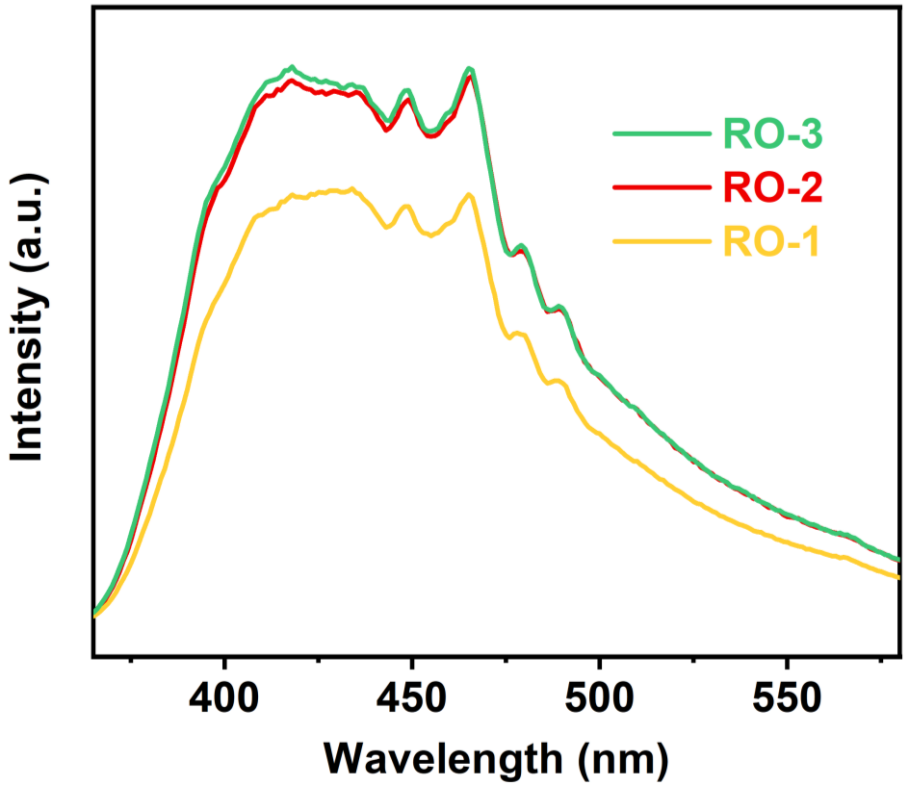

Figure S30. PL emissions of **RO-1, 2, 3** under excitation at 350 nm.

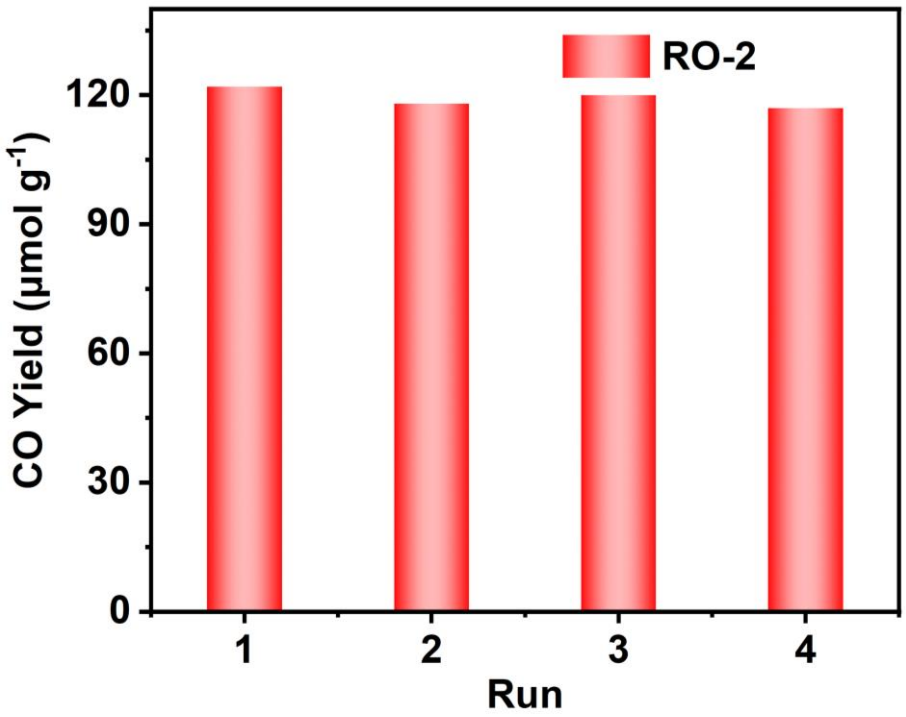

Figure S31. Yield of CO for **RO-2** as CO_2RR photocatalyst in four continuous runs.

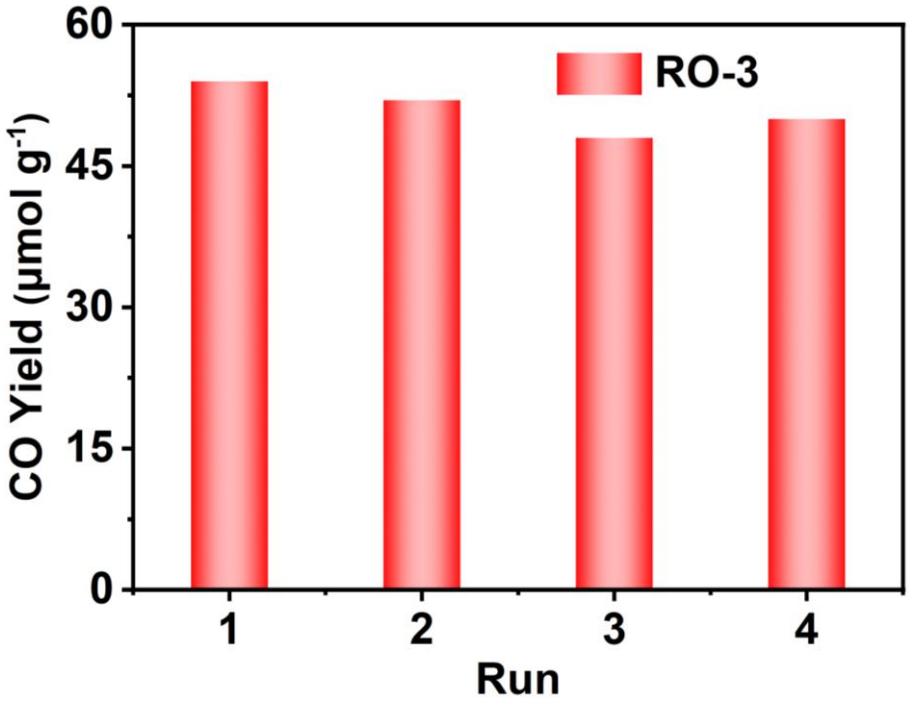

Figure S32. Yield of CO for **RO-3** as CO_2RR photocatalyst in four continuous runs.

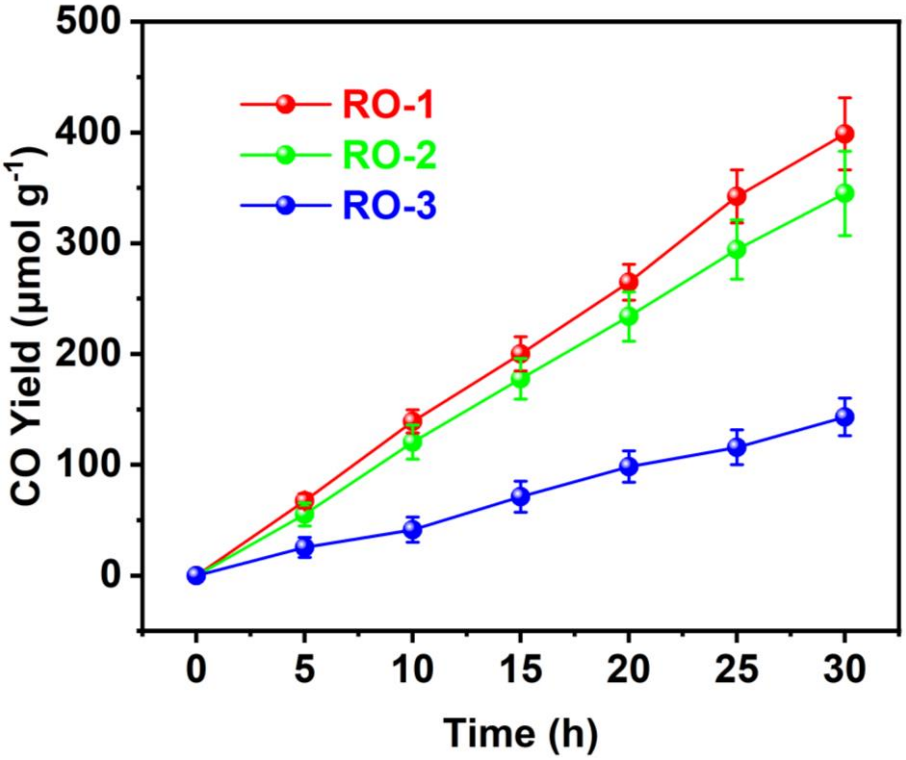

Figure S33. Yield of CO for **RO-1, 2, 3** as CO_2RR photocatalysts in 30 hours.

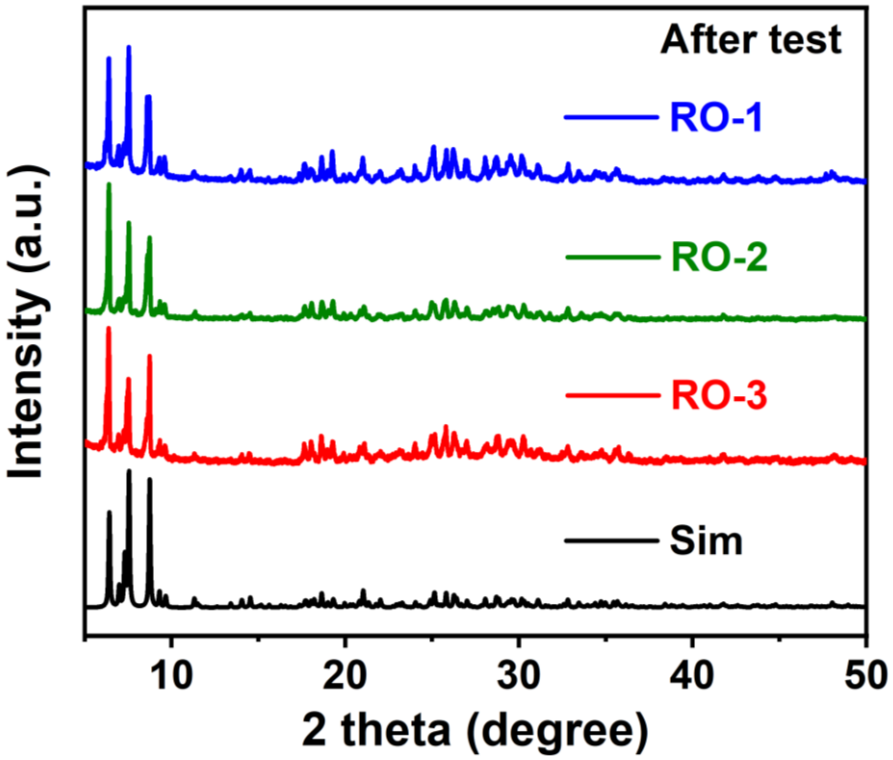

Figure S34. The PXRD patterns of **RO-1, 2, 3** after cyclic test: simulated pattern (black curve), **RO-1** (blue curve), **RO-2** (green curve), **RO-3** (red curve), respectively.

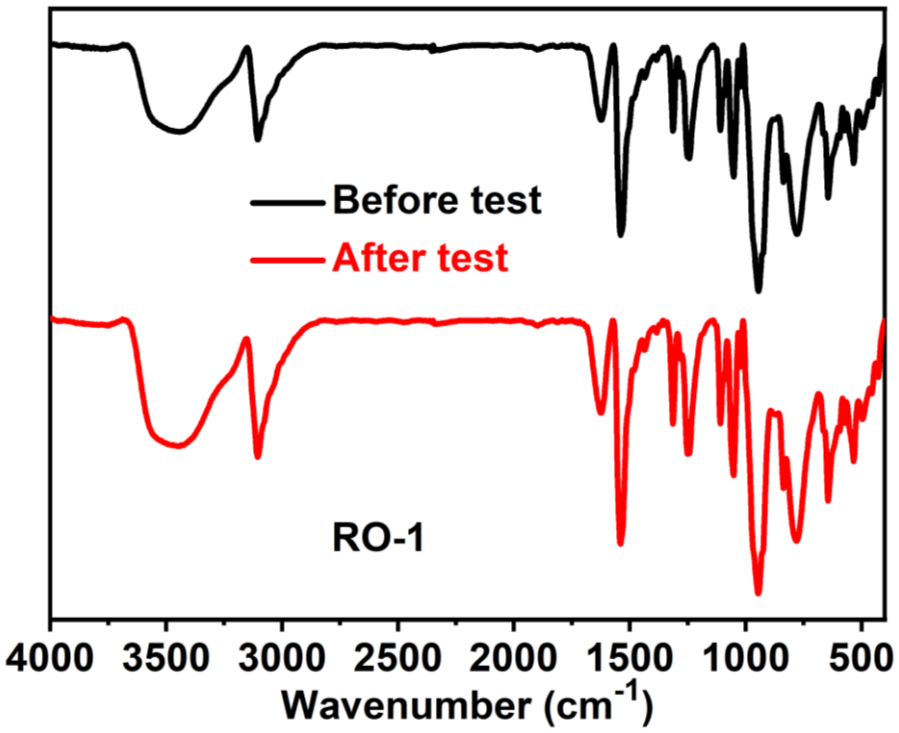

Figure S35. The FTIR spectra for **RO-1** before and after reaction.

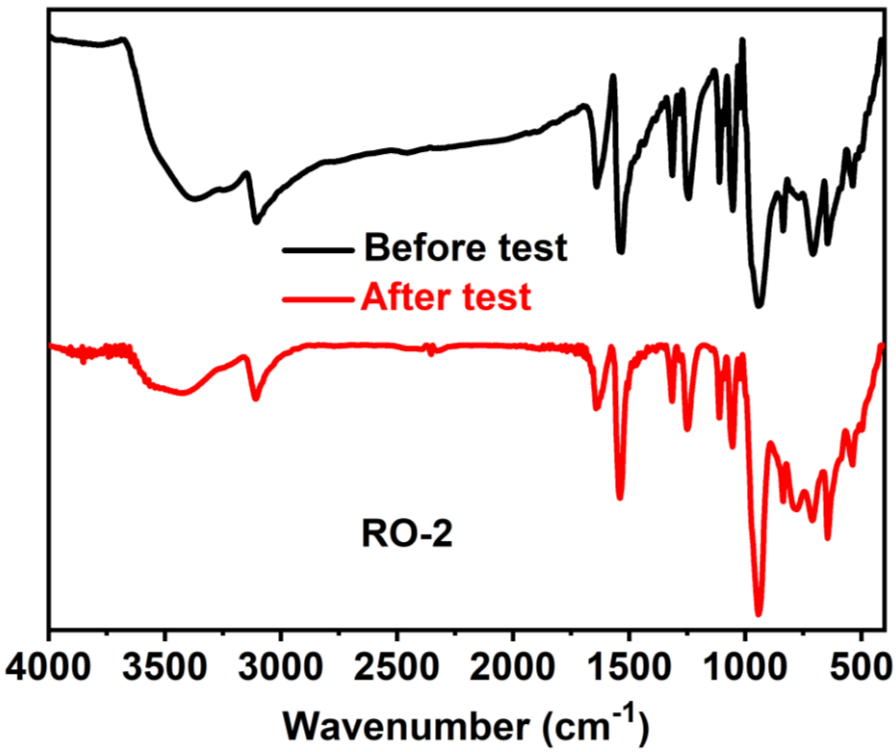

Figure S36. The FTIR spectra for **RO-2** before and after reaction.

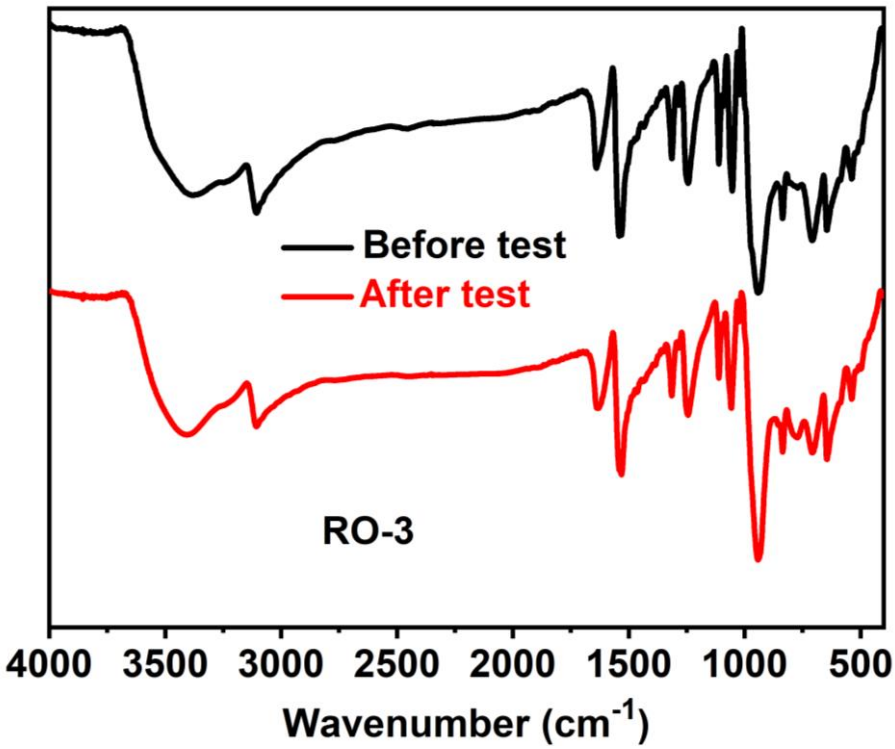

Figure S37. The FTIR spectra for **RO-3** before and after reaction.

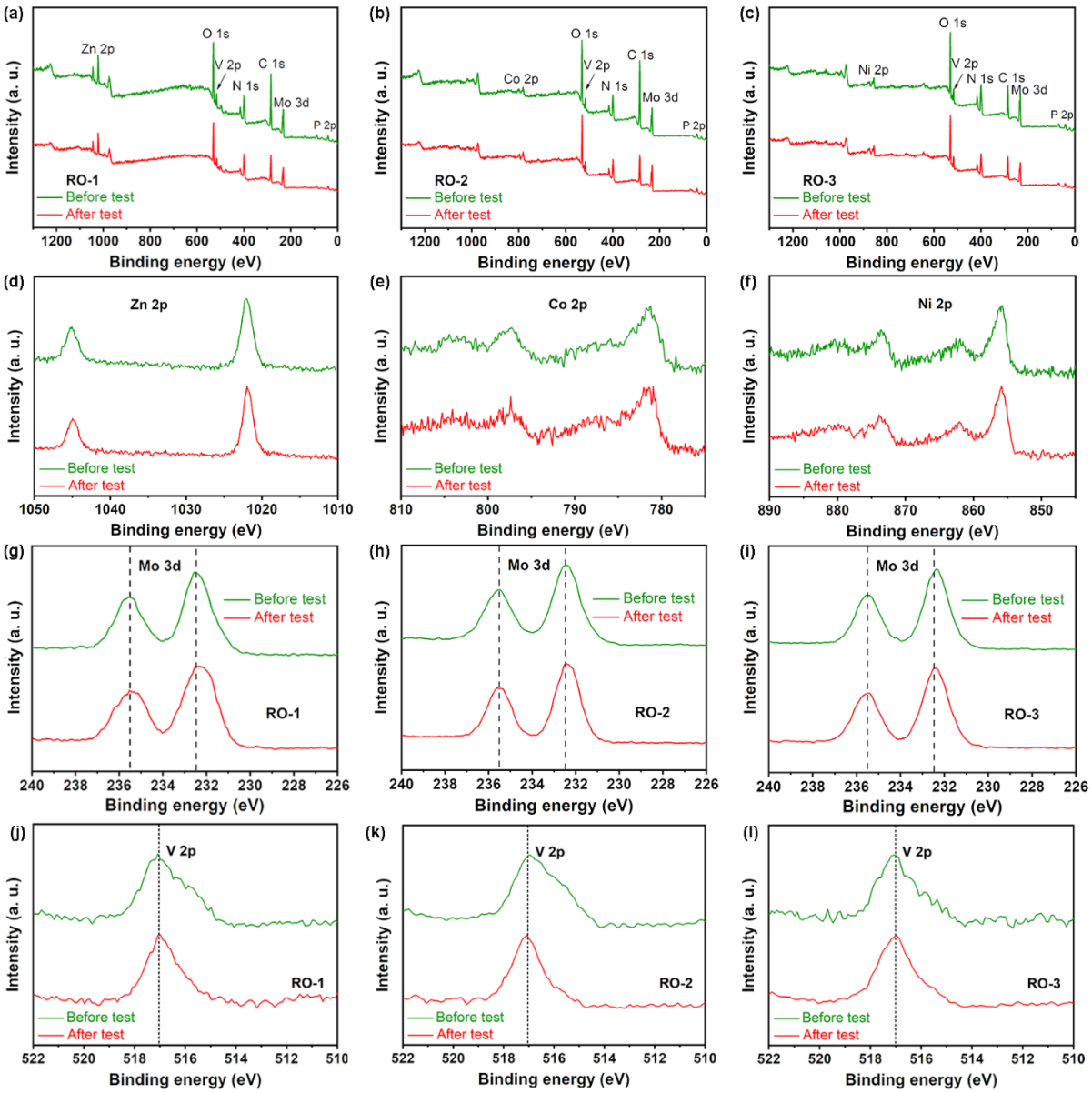

Figure S38. (a~c) The XPS spectra of **RO-1, 2, 3** before and after photocatalysis; The high-resolution peaks of M 2p (d~f), Mo 3d (g~i) and V 2p (j~l) spectrum of **RO-1, 2, 3** before and after photocatalysis, respectively.

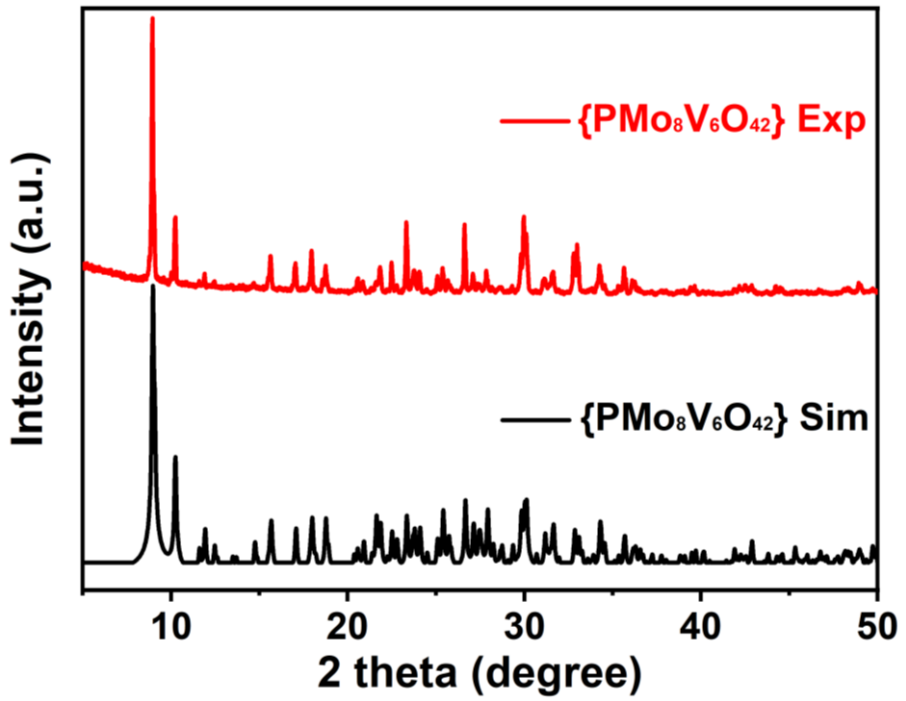

Figure S39. The PXRD pattern of $\{PMo_8V_6O_{42}\}$: simulated pattern (black), experimental pattern (red), respectively.

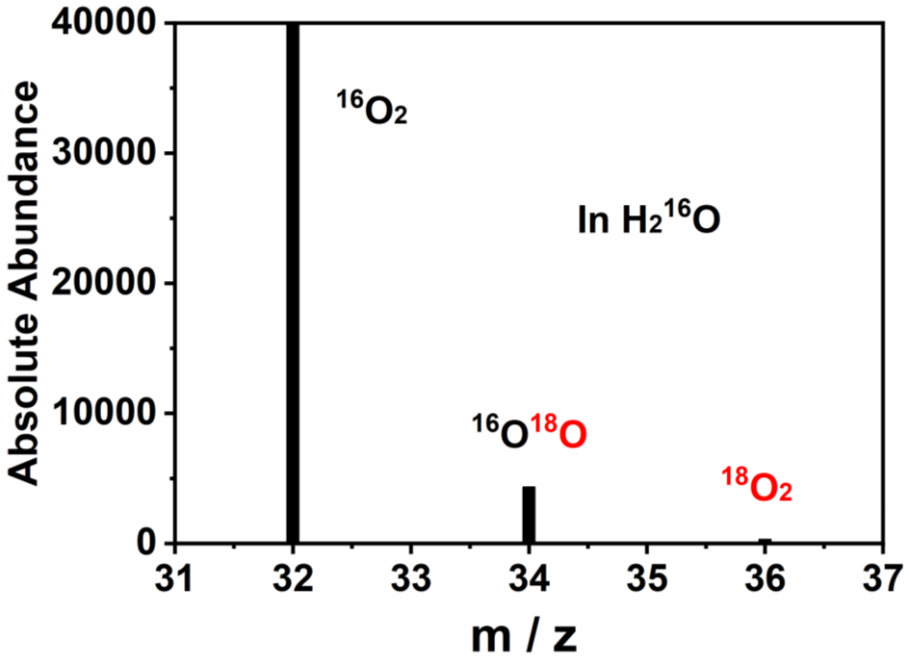

Figure S40. Mass spectrum extracted from GC-MS analysis of O_2 product from $H_2{}^{16}O$ oxidation.

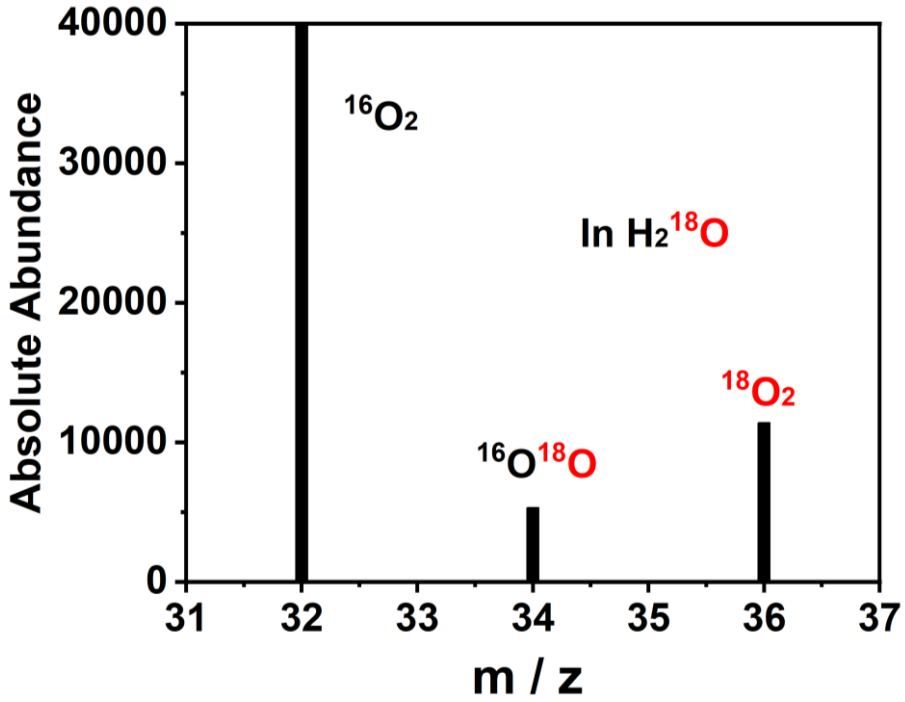

Figure S41. Mass spectrum of product O_2 from the photocatalytic reaction in (a) H_2O and (b) $H_2{}^{18}O$ with **RO-1** as catalyst.

$O^{18}O$ and $^{18}O_2$ were detected as ion monitoring modes. When the photocatalytic reaction occurs in the existence of $H_2{}^{16}O$, the two isotope abundance ratio is 100/7.45 (34:36). This may be attributed to the existence of isotope ^{18}O in water. The isotope abundance ratio in $H_2{}^{18}O$ is 46.67/100 (34:36). The higher the abundance of $^{18}O_2$, indicating that the photocatalytic reaction indeed achieve the H_2O-to-O_2.

Table S2. ICP analysis for **RO-1, 2, 3**.

	Element	**Wt%**	**Atomic ratio**
RO-1	Mo/ V/ Zn	22.90/9.48/6.72	8.5806/6.7059/3.7135
RO-2	Mo/ V/ Co	21.09/10.37/5.42	8.9661/6.9065/3.1274
RO-3	Mo/ V/ Ni	24.69/10.64/5.75	8.6678/7.0305/3.3017

Table S3. A series of contrast experiments based on **RO-1, 2, 3**.

Catalyst	Conditions	CO Yield (umol / g)
RO-1	Normal[1]	138
RO-2		122
RO-3		54
RO-1	Without irradiation	0
RO-1	Without water	2.3
RO-1	Ar replace CO_2	0
$\{PMo_8V_6O_{42}\}$	Normal	55
$H_3PMo_{12}O_{40}\cdot xH_2O$	Normal	43
Physical mixture of V_2O_5 / MoO_3 / $ZnCl_2$ (2 mg / 2 mg / 1 mg)	Normal	30.2
Physical mixture of V_2O_5 / MoO_3 / $CoCl_2$ (2 mg / 2 mg / 1 mg)	Normal	29.6
Physical mixture of V_2O_5 / MoO_3 / $NiCl_2$ (2 mg / 2 mg / 1 mg)	Normal	35
p-tr_2Ph	Normal	0

[1]Reaction condition: catalyst 5 mg, water 200 μL, CO_2 1 bar, irradiation time 10 h.

Theoretical methods and results

Computational methods

Periodic calculations

The structure optimization and free energy calculations were performed within the framework of the density functional theory (DFT) as implemented in the Vienna Ab initio Software Package (VASP 5.3.5) code within the Perdew–Burke–Ernzerhof (PBE) generalized gradient approximation and the projected augmented wave (PAW) method[5-8]. The cutoff energy for the plane-wave basis set was set to 400 eV. The Brillouin zone of the surface unit cell was sampled by Monkhorst–Pack (MP) grids, with a k-point mesh for RO bulk structure optimizations[9]. The **RO-1, 2, 3** bulk was determined by 2 × 2 × 2 Monkhorst−Pack grid. The convergence criterion for the electronic self-consistent iteration and force was set to 10^{-5} eV and 0.01 eV/Å, respectively. The PBE+U approach was applied to calculations of the Mo, Co, Ni-contained systems. In this work, we set the Hubbard parameter to U − J = 5 for Mo, 4 for Co, 6 for Ni, which ensures a good qualitative description of structure and electronic properties.

The free energies of adsorbates at temperature T were estimated according to the harmonic approximation, and the entropy is evaluated using the following equation:

$$S(T) = K_B \sum_{i}^{\text{harm DOF}} \left(\frac{\varepsilon_i}{K_B T (e^{\frac{\varepsilon_i}{K_B T}} - 1)} - \ln\left(1 - e^{-\frac{\varepsilon_i}{K_B T}}\right) \right)$$

where k_B is Boltzmann's constant and DOF is the number of harmonic energies (ε_i) used in the summation denoted as the degree of freedom, which is generally 3N, where N is the number of atoms in the adsorbates. Meanwhile, the free energies of gas phase species are corrected as:

$$G_g(T) = E_{elec} + E_{ZPE} + \int C_p \, dT - TS(T)$$

where C_p is the gas phase heat capacity as a function of temperature derived from Shomate equations and the corresponding parameters in the equations were obtained from NIST.

Model cluster calculations

To perform time-dependent density-functional theory (TDDFT), a model cluster as shown in Figure S41 is contructured based on the optimized structure from periodic calculations. The cluster calculations are done by the ORCA package employing the resolution of identity approximation.[10] The hybrid B3LYP functional was applied with basis sets of def2-SVP[11, 12] for all atoms in the complexes with decontracted auxiliary def2-SVP/J Coulomb fitting basis sets.[13] For TDDFT calculations, the frist 100 excitations are calculated.

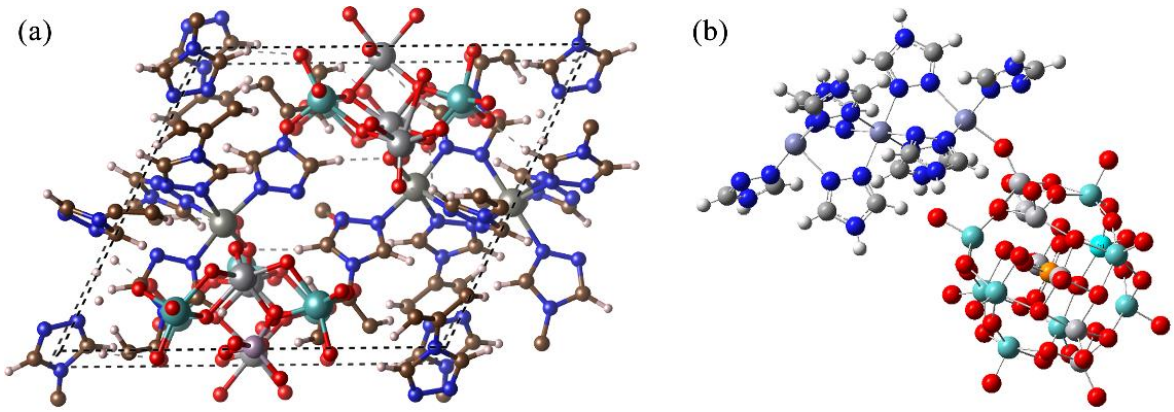

Figure S42. Periodic unit cell and cluster model for DFT and TDDFT calculations.

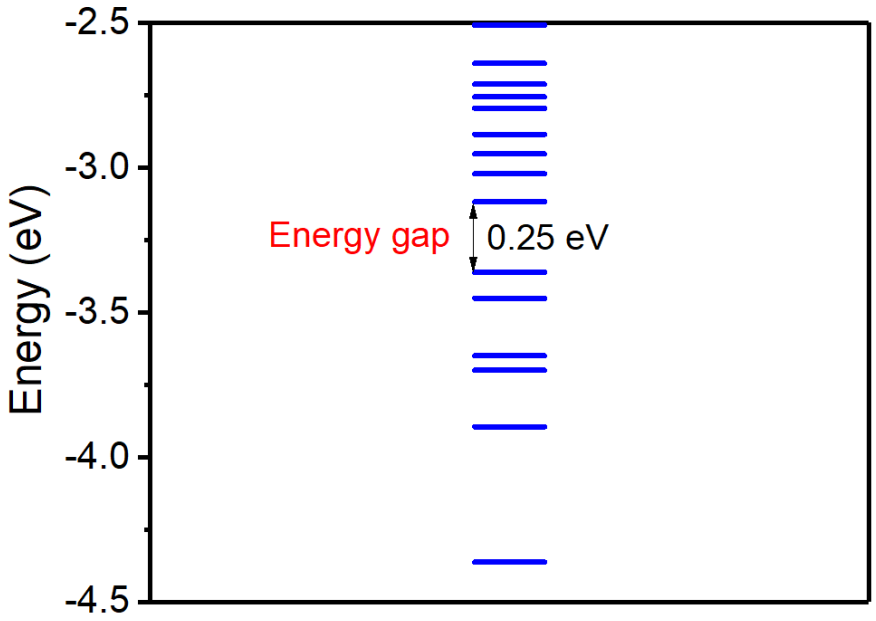

Figure S43. Frotiner energy levels of the model cluster calculated by B3LYP/def2-SVP.

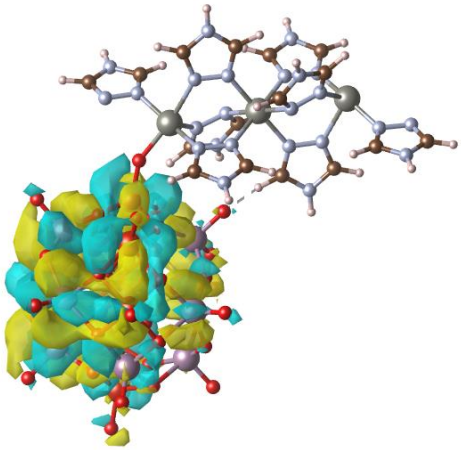	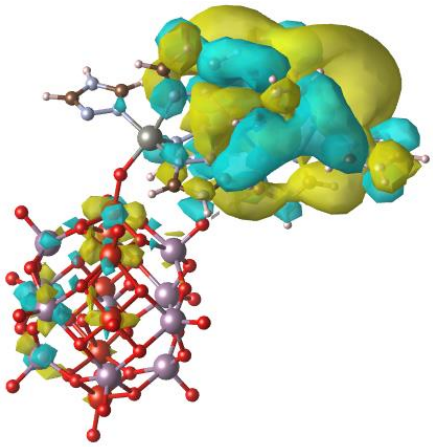
HOMO-4	HOMO-3
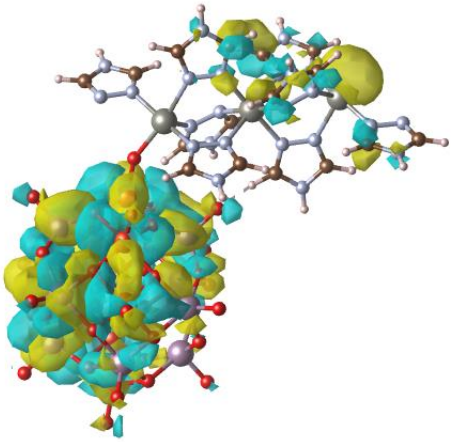	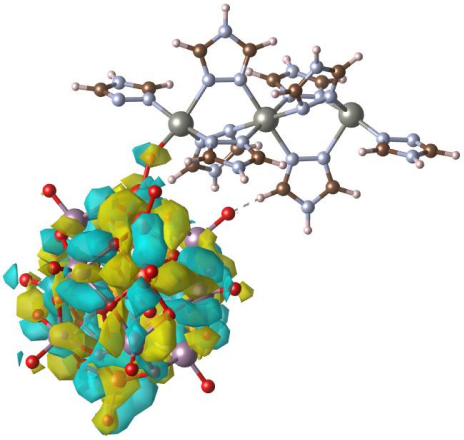
HOMO-2	HOMO-1
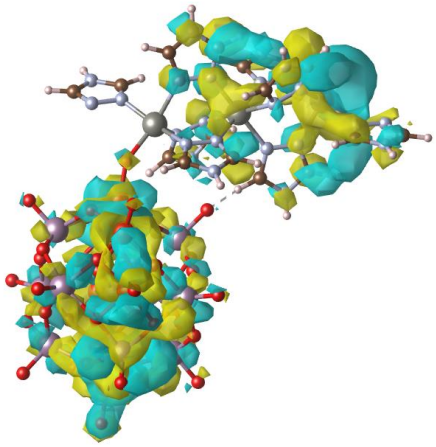	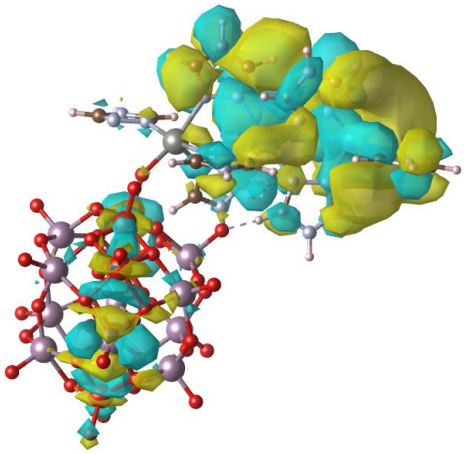
HOMO	LUMO

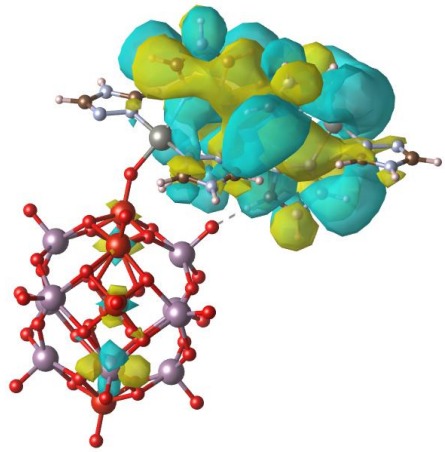	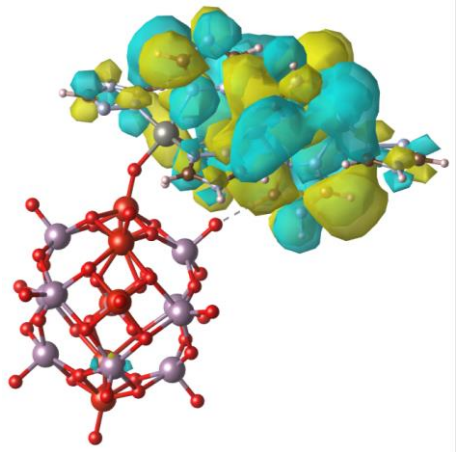
LUMO+1	LUMO+2
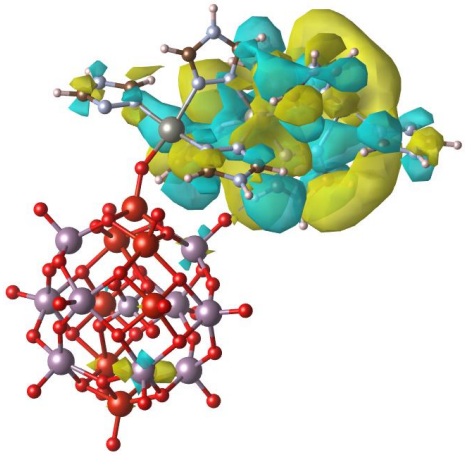	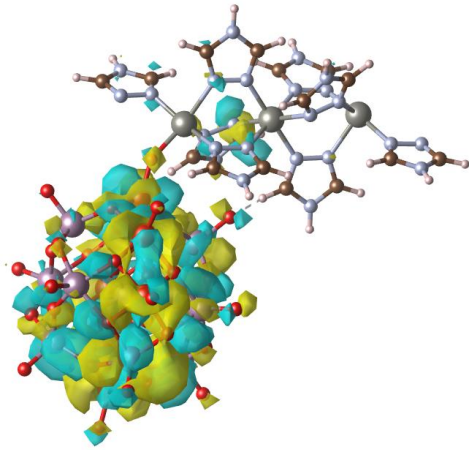
LUMO+3	LUMO+4

Figure S44. Frontier molecular orbital anaylsis of **RO-1** calculated by B3LYP/def2-SVP.

Figure 4b illustrates two types of orbital transitions and the HOMO/LUMO numbers were chosen by the following steps, a) simulate the absorption properties of the target system by TDDFT and list all the electron excitation processes as show in **Figure 4a** (vertical lines); b) choose several electron excitations with large transition dipole moments (I and II in **Figure 4a**), which corresponds to high absorption coefficients. c) analyze the orbital contributions for the selected electron excitations with large coefficients and plot the orbitals out as shown in **Figure 4b**.

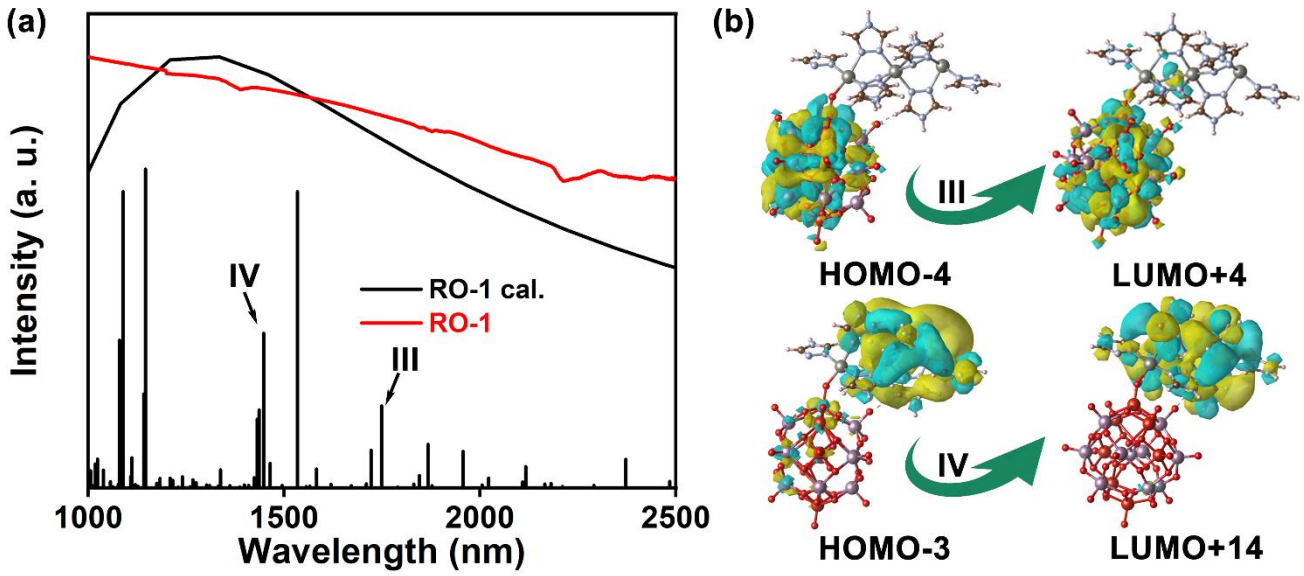

Figure S45. (a) Comparisons of experimental and calculated absorption spectra of **RO-1**. (b) Internal transitions of the {$PMo_9V_7O_{44}$} and the {**M**$_3$}, respectively.

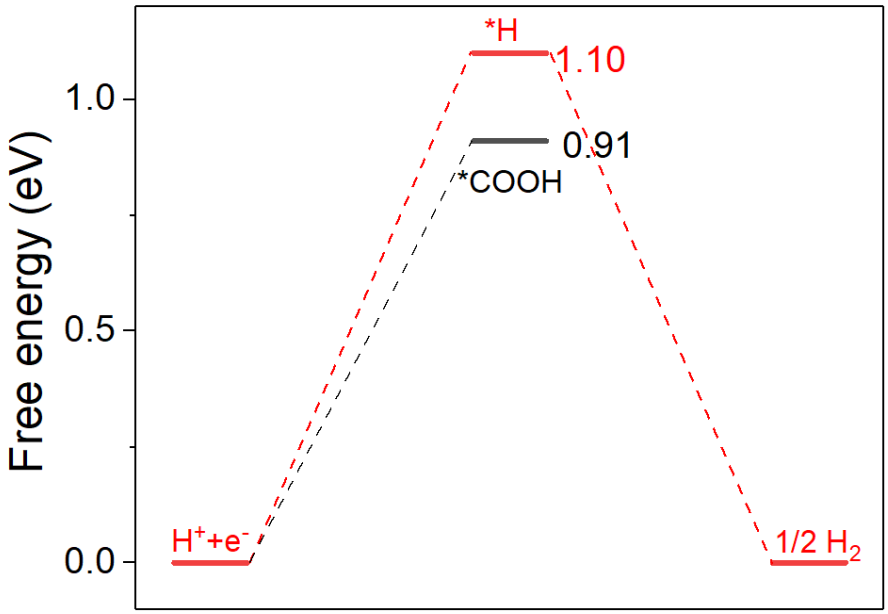

Figure S46. Free energy change for the formation of *H and *COOH on Zn site of **RO-1**.

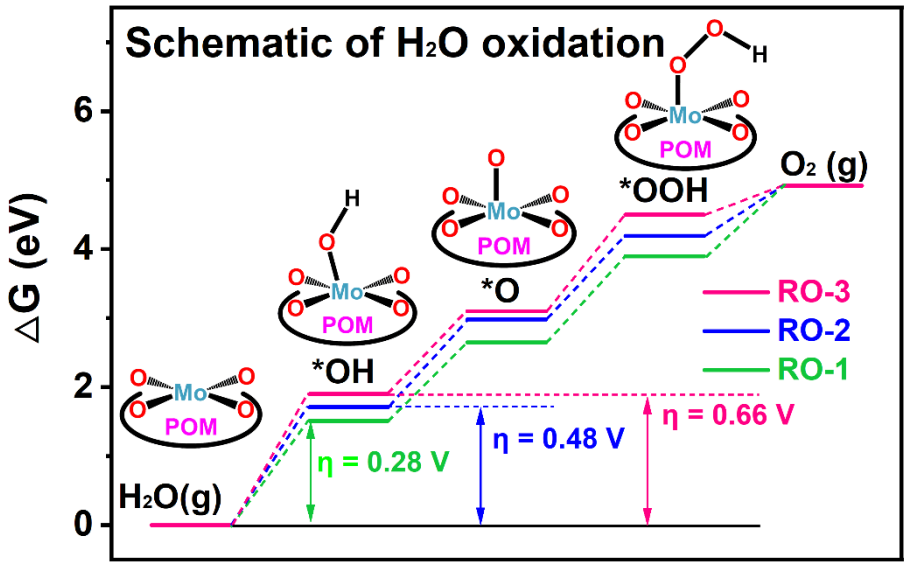

Figure S47. The free-energy profile for the WOR pathway.

Table S4. The energy difference of photocatalytic CO_2RR pathway (1 - 3) and WOR pathway (4 - 7).

	Chemical equation	The energy difference (△G, eV)		
		RO-1	**RO-2**	**RO-3**
1	$CO_{2(g)}+*+H^++e^-\rightarrow *COOH$	0.91233	1.25436	1.8941
2	$*COOH+H^++e^-\rightarrow *CO+H_2O$	-0.12511	-0.29962	-0.62709
3	$*CO\rightarrow CO_{(g)}$	-0.064	-0.23152	-0.54379
4	$H_2O\rightarrow *OH+H^++e^-$	1.51241	1.71258	1.8985
5	$*OH\rightarrow *O+H^++e^-$	1.13328	1.27031	1.20242
6	$*O+ H_2O\rightarrow *OOH+H^++e^-$	1.25346	1.20916	1.4006
7	$*OOH\rightarrow O_{2(g)}+H^++e^-$	1.02085	0.72795	0.41848

References

(1). Markov, V. T.; Fetisov, G. V.; Zhukov, S. G., Correction for absorption and beam inhomogeneity in X-ray single-crystal diffractometry: method of analytical integration. *J. Appl. Crystallogr.* **1990**, *23*, 94-98.

(2). Sheldrick, G., A short history of SHELX. *Acta Crystallogr. Sect. A* **2008**, *64*, 112-122.

(3). Sheldrick, G., Crystal structure refinement with SHELXL. *Acta Crystallogr. Sect. C* **2015**, *71*, 3-8.

(4). Dolomanov, O. V.; Bourhis, L. J.; Gildea, R. J.; Howard, J. A. K.; Puschmann, H., OLEX2: a complete structure solution, refinement and analysis program. *J. Appl. Crystallogr.* **2009**, *42*, 339-341.

(5). Perdew, J. P.; Burke, K.; Ernzerhof, M., Generalized Gradient Approximation Made Simple. *Phys. Rev. Lett.* **1996**, *77*, 3865-3868.

(6). Hammer, B.; Hansen, L. B.; Nørskov, J. K., Improved adsorption energetics within density-functional theory using revised Perdew-Burke-Ernzerhof functionals. *Phys. Rev. B* **1999**, *59*, 7413-7421.

(7). Blöchl, P. E., Projector augmented-wave method. *Phys. Rev. B* **1994**, *50*, 17953-17979.

(8). Kresse, G.; Joubert, D., From ultrasoft pseudopotentials to the projector augmented-wave method. *Phys. Rev. B* **1999**, *59*, 1758-1775.

(9). Monkhorst, H. J.; Pack, J. D., Special points for Brillouin-zone integrations. *Phys. Rev. B* **1976**, *13*, 5188-5192.

(10). Neese, F., The ORCA program system. *WIREs: Comput. Mol. Sci.* **2012**, *2*, 73-78.

(11). Schäfer, A.; Huber, C.; Ahlrichs, R., Fully optimized contracted Gaussian basis sets of triple zeta valence quality for atoms Li to Kr. *J. Chem. Phys.* **1994**, *100*, 5829.

(12). Weigend, F.; Häser, M.; Patzelt, H.; Ahlrichs, R., RI-MP2: optimized auxiliary basis sets and demonstration of efficiency. *Chem. Phys. Lett.* **1998**, *294*, 143-152.

(13). Weigend, F., Accurate Coulomb-fitting basis sets for H to Rn. *Phys. Chem. Chem. Phys.* **2006**, *8*, 1057-1065.